

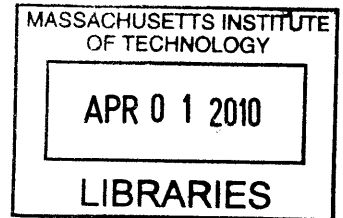
Quantitative analysis of axon elongation: A novel
application of stochastic modeling techniques to
long-term, high-resolution time-lapse microscopy of
cortical axons

by

Neville Espi Sanjana

B.S., Symbolic Systems, Stanford University (2001)

A.B., English, Stanford University (2001)



ARCHIVES

Submitted to the Department of Brain & Cognitive Sciences
in partial fulfillment of the requirements for the degree of


Doctor of Philosophy in Neuroscience

at the

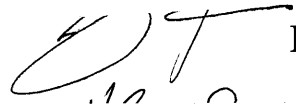
MASSACHUSETTS INSTITUTE OF TECHNOLOGY

February 2010

© Massachusetts Institute of Technology 2010. All rights reserved.

Author 

Department of Brain & Cognitive Sciences
December 17, 2009

Certified by 

H. Sebastian Seung
Professor of Computational Neuroscience
Thesis Supervisor

Accepted by 

Earl K. Miller
Picower Professor of Neuroscience
Chairman, Department Committee on Graduate Theses

Quantitative analysis of axon elongation: A novel application of stochastic modeling techniques to long-term, high-resolution time-lapse microscopy of cortical axons

by

Neville Espi Sanjana

Submitted to the Department of Brain & Cognitive Sciences
on December 17, 2009, in partial fulfillment of the
requirements for the degree of
Doctor of Philosophy in Neuroscience

Abstract

Axons exhibit a rich variety of behaviors, such as elongation, turning, branching, and fasciculation, all in service of the complex goal of wiring up the brain. In order to quantify these behaviors, I have developed a system for in vitro imaging of axon growth cones with time-lapse fluorescence microscopy. Image tiles are automatically captured and assembled into a mosaic image of a square millimeter region. GFP-expressing mouse cortical neurons can be imaged once every few minutes for up to weeks if phototoxicity is minimized.

Looking at the data, the trajectories of axon growth cones seem to alternate between long, straight segments and sudden turns. I first rigorously test the idea that the straight segments are generated from a biased random walk by analyzing the correlation between growth cone steps in the time and frequency domain. To formalize and test the intuition that sharp turns join straight segments, I fit a hidden Markov model to time series of growth cone velocity vectors. The hidden state variable represents the bias direction of a biased random walk, and specifies the mean and variance of a Gaussian distribution from which velocities are drawn. Rotational symmetry is used to constrain the transition probabilities of the hidden variable, as well as the Gaussian distributions for the hidden states. Maximum likelihood estimation of the model parameters shows that the most probable behavior is to remain in the same hidden state. The second most probable behavior is to turn by about 40 degrees. Smaller angle turns are highly improbable, consistent with the idea that the axon makes sudden turns. When the same hidden Markov model was applied to artificially generated meandering trajectories, the transition probabilities were significant only for small angle turns.

This novel application of stochastic models to growth cone trajectories provides a quantitative framework for testing interventions (eg. pharmacological, activity-related, etc.) that can impact axonal growth cone movement and turning. For example, manipulations that inhibit actin polymerization increase the frequency and angle of turns made by the growth cone. More generally, axon behaviors may be useful in deducing computational principles for wiring up circuits.

Thesis Supervisor: H. Sebastian Seung
Title: Professor of Computational Neuroscience

Acknowledgements

All of this work has been done in collaboration with my advisor Sebastian Seung, whom I will say more about below. Jeannine Foley and Heather Sullivan cultured the amazing GFP mixture cultures, which were made from transgenic mice that Candy Carr was so kind to breed and share with us.

My advisor, Sebastian Seung, has been a wonderful guide and friend on this graduate school journey. Although the journey has had its share of missteps and projects that didn't quite work out, he always remained enthusiastic and hungry for the best science that we could possibly do. (And I hope this thesis represents some of that.) From my first weeks in the lab, Sebastian made it clear that the only limit in science is our own imagination. Whether it was arguing over equivalent circuit diagrams at Tosci's or tearing down an ineffectual Faraday cage, Sebastian was always confident that we could figure things out by thinking and reasoning on our own. I don't think I'll ever forget my elation following recording from the first neuron patched in the lab (by Sebastian at our single shared experimental rig). I learned through that experience and others in my first year that I could teach myself new skills and learn independently. And that that hard fought knowledge is often the most solid.

This seemingly obvious revelation has had deep reverberations in all aspects of my life, scientific and otherwise. Frankly, it's difficult sometimes to recall life before joining the Seung Lab because I have been changed so greatly from those experiences. Sebastian's can-do attitude has taken root in me and I can say, due to his examples, I have become fearless, taking on the challenges of learning new techniques on my own and being the first to perform them in our lab.

Never one for complacency or lax thinking, Sebastian leads primarily by example. I think it says volumes about that example that his students and postdocs often adopt his rhetorical style and direct, penetrating questions. Perhaps the greatest gift I have from Sebastian is an appreciation of the incomparable joys of a life of science. His love of it must be contagious. I came into graduate school utterly convinced that academia was not the place for me, but the excitement of neuroscience cultivated in the Seung Lab has spun me around 180 degrees. To live a life of the mind (literally) would be an amazing privilege.

I would also like to thank my thesis committee. Although I only recently have come to know Mehran Kardar, I am deeply impressed by him. From the beginning, he has been wonderful, providing many insightful comments and reminding me to stay focused on the most interesting results.

Martha Constantine-Patton provided perhaps the earliest encouragement of anyone at MIT – in a note on the corner of my first midterm – and gave me the confidence early on to believe that I could be a capable scientist and thinker. She has impressed upon me that regardless of what stage one is at in his or her scientific career, it is always a good thing to ask questions and that a complete understanding is vital to the dissemination of ideas.

Carlos Lois has been like a second advisor to me – a true mentor in many ways. Years ago, he was willing to take a chance on me by allowing me to learn molecular neurobiology as a teaching assistant in his laboratory course. He could easily have found a more experienced TA but was good enough to let me learn on the job. I only hope that my recent, independent molecular foray into the world of RNA editing will prove his gamble to be a worthwhile one. I owe him a huge debt of gratitude for the skills that I learned at that time and have put to

much use since. Carlos embraces scientific honesty like no other: His criticisms have helped awaken in me a self-critical nature that is vital for any scientist. As if knowing that criticism alone is unhelpful, Carlos is also a fount of creativity, constantly encouraging me to "imagine, imagine" (with a Spanish accent!) one experiment or another. His amazing openness and desire to share knowledge has helped me immensely and continues to help me. Carlos, with luck, I hope to one day tell you that I too am a "pipetting PI".

In our graduate office, Denise Heintze and Brandy Baker have had a lasting influence by not just taking care of administrative hassles whenever and wherever they arose but by also providing a sympathetic ear when needed. In particular, Denise has been a true advocate for graduate students, a group whose concerns and needs often go unheard.

In the Seung Lab, getting things done has been easy due to the tireless efforts of Amy Dunn. She makes the lab run smoothly and that's not easy.

There are many friends who've been there along the way. My three classmates – Jennifer Wang, Emily Hueske, and Tevya Rachelson – have become some of my closest friends in life and I am unbelievably lucky to have met them. None of my time in graduate school would have been so enjoyable without a little help from my friends. And I am indebted to the support of so many caring friends. It hardly does justice to just list them but nonetheless: Nathan Wilson, Dana Hunt, John Choi, Artem Starovoytov, Sami Amasha, Viren Jain, Srini Turaga, Sabrina Spencer, Leeland Ekstrom, Peter Bermel, Alex Shalek, Jacob Robinson, Erez Levanon, Billy Li, Risa Kawai, Jessi Ambrose, Sawyer Fuller, Aleem Siddiqui, Mark Goldman, Russ Tedrake, Ila Fiete, Seungeun Oh, Josh Tenenbaum, Denise Heintze, Brandy Baker, Kay-chi Leung, Li-li Harn, Dave Sherman, Cassandra Munson, Eloy Martinez, Nupur Lala, Ulysses Lateiner, Ben Scott, Aaron Andalman, Tom Davidson, David Nguyen, Mike Long, Jessie Goldberg, Retsina Meyer, Rebecca Sutherland, Mark Histed, Talia Konkle, Michael Frank, Kartik Ramamoorthi, Yingxi Lin.

Finally, I would like to thank my parents: Veera and Espi Sanjana. They have been incredibly supportive and understanding at all times, which has set an extraordinary example.

Contents

1	Introduction	7
1.1	Thesis organization	8
1.2	A brief history of watching axons elongate	9
1.2.1	Early work: Basic quantitative measures of axons and a qualitative description of growth cone advance using VEC-DIC	9
1.2.2	More sophisticated quantitative models: Random walks and fractal dimensions	10
1.2.3	Fluorescence microscopy 1: The cytoskeleton	12
1.2.4	Fluorescence microscopy 2: Labeling synapses with fusion proteins and mammalian neocortex in vivo	13
1.2.5	Chemoreception models of axon dynamics	14
1.2.6	Summary	15
1.3	Towards a quantitative framework for axon elongation	15
2	Long-term fully-automated time-lapse of growing axons for weeks	17
2.1	Primary cortical neuron mixture culture	18
2.2	Time-lapse imaging	18
2.3	Image alignment and growth cone tracking	20
3	Quantitative analysis of axon elongation: Steps and stochastic models	21
3.1	Time series of velocity vectors	21
3.2	Mean and covariance of the velocity	21
3.3	Temporal correlations of the velocity	22
3.4	Biased random walk model	23
3.5	Changes in the bias	23
3.6	Hidden Markov model	24
3.7	Automatic segmentation and parameter learning	25
3.8	Results of the HMM	25
3.9	Validating the model	26
3.10	Bias versus persistence	27
3.11	Retractions	28
3.12	Stochastic modeling methods	28
3.13	Figures	29
4	Using stochastic modeling to detect changes in elongation behavior	41

5	Conclusion	47
5.1	Interpretations of the hidden state	47
5.2	What is the cause of straightness?	48
5.3	Straightness as a metabehavior of elongation	48
5.4	In vivo vs. in vitro	49
5.5	Stochastic models for quantifying cellular behavior	49
6	Appendix: A fast flexible ink-jet printing method for patterning dissociated neurons in culture	50
	Bibliography	64

Chapter 1

Introduction

This thesis is about the behaviors of elongating axons. I present a unified experimental and theoretical framework for recording, describing and quantifying these elongation behaviors. The major contributions of the thesis are:

- Construction of an optimized imaging platform for fully-automated, high-resolution fluorescence microscopy of growing axons for days to weeks at high temporal resolution.
 - Key innovations include autofocus (evaluation function and search), phototoxicity reduction, environmental control, hardware and software control and automation with an emphasis on fault-tolerance and stability.
- Acquisition of long-term time-lapse movies of cultured primary rodent cortical neurons over a large area ($\sim 1\text{mm}^2$) for an unprecedented duration (weeks). Pixel resolution is sub-micron with a standard single frame size of 30 megapixels.
- A rigorous examination (and confirmation) of the prevailing – yet heretofore poorly supported – claim that axon elongation precedes as a biased random walk (BRW), i.e. after subtracting an average velocity (“bias”), individual elongation steps are statistically independent.
- A novel description and unification of axon elongation behavior at short (minutes to hours) and long (hours to days) timescales. The BRW is a good description at the short timescale but at longer timescales axons turn and change their growth direction before again proceeding to elongate in a BRW.
- A novel application of stochastic modeling techniques for quantitative analysis of axon growth cone trajectories:
 - The dynamics of the bias direction is modeled as the hidden state of a hidden Markov model (a simple dynamic Bayesian network).
 - Dynamic programming techniques (eg. Viterbi algorithm) can be used to both estimate the most likely bias direction dynamics and estimate the optimal model parameters. The model parameters are the mean and variance of the BRW steps and the distribution of turning directions between BRWs.

- The model parameters and related statistics can be considered a new assay for neurite guidance that provides a fundamentally different type of information about growth cone trajectories.
 - A manipulation for the assay: The HMM is used to quantify changes in the growth cone trajectory when F-actin depolymerizing drugs are applied to the axons. Upon examination, these drugs affect the BRW duration and the turn distribution (both the probability and symmetry of turns).

1.1 Thesis organization

This thesis describes novel experimental and theoretical techniques for quantifying axon elongation. To provide appropriate context, this introductory chapter briefly reviews the relevant literature from the past 40 years of axon elongation studies. This period coincides with the beginning of *quantitative* description of axon growth cone movement. The review emphasizes two themes: 1) the parallel development of improved biological descriptions with new microscopy techniques; and 2) biological constraints on axon elongation that result directly from observations and quantitative description.

The rest of the thesis (aside from the Appendix, see below) is drawn from a single research article in preparation. The remainder of the introductory chapter motivates my work on a new kind of quantitative description of axon elongation and why stochastic modeling techniques are the right tools for the job.

In Chapter 2, I present the experimental methods that enable high-resolution, long-term time-lapse of axons. This includes the primary cortical neuron transgenic mixture culture for labeling and the technical innovations for fully automated time-lapse imaging. I also discuss other practical aspects of gathering growth cone trajectories: image alignment and growth cone tracking, and basic quantitative measures of axon growth.

To analyze the (over)abundance of data from these time-lapse movies, I focus on two questions in Chapter 3. Do axons perform a biased random walk as they elongate? And, if so, how does the bias direction change over longer timescales? The first question is addressed through testing necessary conditions for a random walk using both time and frequency domain measures. The second question is answered through the application of the hidden Markov model formalism and related inference algorithms to the axon growth cone data. In Chapter 4, I discuss the use of the hidden Markov model to detect changes in the axon growth cone trajectory associated with a cytoskeletal manipulation.

I conclude in Chapter 5 with a discussion of some of the implications of the quantitative analysis of axon elongation, including possible biological interpretations for the dynamics of the hidden variable. The appendix (Chapter 6) was previously published as Sanjana and Fuller (2004) and is included here because the novel experimental setup described in the thesis grew from an imaging platform built during that work on cell patterning and growth control.

1.2 A brief history of watching axons elongate

1.2.1 Early work: Basic quantitative measures of axons and a qualitative description of growth cone advance using VEC-DIC

The growth cone was first described by Ramon y Cajal in embryonic spinal cord in 1890 (Dent and Gertler, 2003). A few years later, cell culture pioneer Harrison was the first to see moving growth cones and Speidel confirmed the observation in the living embryo. Quantitative observation of axon movement entered a golden age in the 1980s and slowly transitioned into a more molecular analysis of cytoskeletal proteins in the 1990s and 2000s.

This golden age of observation was largely possible due to new microscopy techniques. But before these innovations appeared there was already a small literature of time-lapse observations of individual growth cones in vitro. A decade earlier Bray elegantly demonstrated that the growth cone is the site of new membrane addition by sprinkling fine glass particles on cultured rat sympathetic neurons to see if the particles on the axon moved as the axon elongated (Bray, 1970). Previously, it was known that chick DRG axons continue to elongate after axotomy (Hughes, 1953) but this demonstrated conclusively that new plasma membrane is added at the growth cone and not at the cell body. Recent work using optical tweezers confirmed this and further showed that the growth cone itself has quite a bit of “slack” membrane (Bray, 1996). The first quantitative time-lapse studies of axon growth from individual neurons in culture were focused primarily on quantifying growth rates (Bray, 1973; Argiro and Johnson, 1982). Through the course of my literature survey, this was the most commonly quantified data, so I kept track of axon outgrowth rates in various systems and they are summarized in the table below.

Organism		Axon growth speed (um/hr)	Reference
Rat superior cervical ganglion	E17	6-13	(Argiro and Johnson, 1982)
	perinatal	15-28	
	adult	3-7	
Chicken dorsal root ganglia		20	(Katz et al., 1984)
Frog	neural tube	25	
	regenerate post-axotomy	16	
Chicken sensory ganglia		65	(Bray and Chapman, 1985)
Aplysia B1 and B2 neurons (buccal ganglia)		5-25	(Goldberg and Burmeister, 1986)
PC12 neuroblastoma cell line		20	(Aletta and Greene, 1988)
Rat superior cervical ganglion		18	
Frog neural tube		70-250	(Tanaka and Kirschner, 1991)
Hamster cortical slice	tract	78	(Halloran and Kalil, 1994)
	sub-target	45	
	target	42	
Chicken dorsal root ganglia		55	(Williamson et al., 1996)
Mouse thalamocortical postnatal		up to 35	(Portera-Cailliau et al., 2005)

Table 1: Compiled list of growth speeds (when given) in cited literature.

Initial attempts to quantify growth cone behavior focused on basic morphological measures and their relationship to the speed of axon outgrowth. Rat superior cervical ganglia growth cones display a fan-like morphology with large lamellipodia during periods of fast advance (>100 um/hr) and a tree-like morphology with mostly filopodia protruding during

slower translocation (Argiro et al., 1984). Also, their filopodia have an exponentially declining rate of extension with the initial rate of extension highly correlated with the final length of the filopodium (Argiro et al., 1985). Filopodia from chicken sensory ganglia sweep over, on average, 65 degrees in a 4.5 minute lifetime (Bray and Chapman, 1985). From a technological standpoint, it is worth mentioning that all of these studies employed existing phase-contrast microscopy, which, as the authors remark, can make observation of single filopodia and of axons among multiple neurites difficult due to the large phase halos generated.

The first technological breakthrough for axon observation was video-enhanced contrast-differential interference contrast (VEC-DIC) microscopy, which is capable of visualizing $<50\text{nm}$ structures, well below the diffraction limit of light microscopy (Langford, 2001). Goldberg and Burmeister used VEC-DIC on the giant growth cones of the sea hare *Aplysia* to first describe what has now become the standard model of axon elongation: 1) lamellipodial veils extend, most often between two adjacent filopodia; 2) vesicles fill the veil; 3) the veil enlarges as it is filled with organelles and more vesicles; and 4) consolidation into the cylindrical shape of the axon (Goldberg and Burmeister, 1986). VEC-DIC lead to similar descriptions of axon advance in PC12 and rat superior cervical ganglion cultures with further quantification of filopodia behaviors, including delineation of two categories of filopodia based on length and lifetime (Aletta and Greene, 1988). Longer filopodia tend to have longer lifetimes. Also significant is that the VEC-DIC observations showed that forward advance is not primarily due to the growth cone itself pulling the axon, as had been long believed, but rather the most significant factor is lamellipodial advance.

1.2.2 More sophisticated quantitative models: Random walks and fractal dimensions

Contemporaneous with the VEC-DIC observations, Katz and colleagues published a series of papers applying more sophisticated metrology and modeling techniques to growing axons (Katz et al., 1984; Katz, 1985b; Katz and George, 1985; Katz, 1985a; George et al., 1988). They used time-lapse observations of cultured frog and chick sensory neurons to fit specifically the elongational movement of the growth cone with a biased random walk (binomial) model (Katz et al., 1984). During my literature search, this work was the most similar to my own thesis project, so I will explain it in greater detail.

Elongational movement is defined as movement requiring a change in axonal length and it is calculated by measuring the orientations of the distal axon and of the growth cone with respect to the last movement. The motivation for separating elongational growth from non-elongational motility is that average short-term (10 minute sampling interval) growth rates were almost double long-term (≥ 1.5 hour sampling interval) growth rates. Considering only elongational short-term growth, they found that short term rates accorded well with long-term growth rates. Also, between observations, the elongation calculation assumes that changes in growth cone orientation occur at a constant rate, which others have found is not always the case (Argiro et al., 1985).

Over the short observations periods ($\sim 3\text{-}4$ hours), growth cones were found to move along relatively straight paths. So, the elongational movement was fitted with a 1-D biased random walk model. The primary motivation to make a model is prediction: to “calculate the

expected proportion of axons undergoing any specific amount of elongation” (Katz et al., 1984). This biased random walk model, which fits a binomial distribution to the elongation observed at each 10-minute interval, is based on two major assumptions. First, the elongation steps are independent. Second, the axon elongates in discrete steps. Others have observed saltatory axon growth (Aletta and Greene, 1988; Halloran and Kalil, 1994), but it is unclear from the methodology whether the particular binomial parameters (which includes a relatively large number of random walk “steps” during each 10 minute interval) provide a significantly better fit than competing parameterizations (eg. with a smaller number of steps and a large step size). In the paper’s discussion, possible biophysical mechanisms to relate to the model’s binomial parameters are given: The step size could reflect the effective growth cone size over which filopodia can extend and the step rate could be determined by the time course of filopodial contraction to overcome internal tension. As mentioned above, filopodial contraction is not the primary method of locomotion: Growth cone advance is mostly due to lamellipodial expansion.

The same authors extended the idea of axons growing relatively straight by quantifying the fractal dimension of observed growth paths (Katz, 1985b; Katz and George, 1985). Fractal dimension is a measure of how completely an object fills the space it is in. In a plane, a straight line has a low fractal dimension, whereas a 2D random walk has a larger fractal dimension. The primary result is that the fractal dimension of the frog and chicken axon growth paths was significantly different from the fractal dimension of a 2D random walk. Also, growth cones were found to actively alternate between leftward and rightward movement more than one would expect to see by chance, implying a preference for staying on a straight trajectory (Katz, 1985b).

But there are some notable issues with calculating the fractal dimension D . Although dimensionless, D was shown to depend on the number of growth cone observations used to calculate it (Katz and George, 1985). In more recent years, several critiques of using fractal dimension to describe animal movements (and, by extension, cellular movements) have appeared (Turchin, 1996; Benhamou, 2004). The fundamental assumption in fractal analyses is that D is a scale-independent parameter, but there are simple, reasonable models for which this assumption is violated. For example, a correlated random walk looks like linear movement ($D=1$) at small spatial scales and like Brownian motion ($D=2$) at very large scales. Katz and colleagues are reasonably rigorous with their use of fractal dimension by calculating the fractal dimension from specific simulated random walks, but, as Turchin suggests, “an alternative approach employing random-walk models provides a more powerful framework for translating individual movements in heterogeneous space into spatial dynamics of populations” (1996). It is worth noting that straightness itself is a very difficult quantity to estimate reliably (Gottfried, 2007) and this is one of the primary issues that our stochastic modeling addresses. Lastly, a similar approach to fractal dimension (Hausdorff dimension) was applied to cultured cat retinal ganglion cells to argue for an intrinsic growth strategy that is non-trivial and results in uniform, space-filling dendritic arbors similar to what is seen in vivo (Montague and Friedlander, 1989).

1.2.3 Fluorescence microscopy 1: The cytoskeleton

The second major microscopy breakthrough was the development of fluorescent labeling of just a few axons using lipophilic membrane dyes (DiI/DiO) and fluorescent tubulin, which incorporates into the microtubule core of axons. In one of the first studies of axon dynamics in situ, hamster cortical slices with DiI-labeled axons crossing to the contralateral hemisphere were imaged to analyze axon behaviors in 3 regions: tract (corpus callosum), subtarget (corpus callosum beneath the cortex contralateral to the injection site), and target (contralateral cortex) (Halloran and Kalil, 1994). Axons were observed for 3-11 hours with a temporal resolution of 16 minutes between images. There were significant differences in axon growth depending on the location that axons were growing. Extension speeds were greatest in the tract and slightly more than half as fast in subtarget and target regions. Axons spent the least time in forward advance in the subtarget region, where the most dramatic behaviors were repeated growth cone collapse and retraction. Interestingly, turning from the subtarget region into the target cortical area was never observed and subsequent work showed that interstitial branching following by regression of the original, mistargeted axon is how this connection is formed (Kuang and Kalil, 1994; Dent et al., 2003).

Starting in the early 1990s, the use of fluorescent tubulin connected observations of axon movement with the dynamics of the core cytoskeletal component of axons, microtubules. Shortly before, it was recognized that the growth cone was the major site of microtubule assembly during axon growth (Bamburg et al., 1986). Fluorescent labeling showed that both microtubules and actin filaments are dynamic structures that are constantly reassembled along the length of the axon (Okabe and Hirokawa, 1990). In a series of papers, Kirschner and colleagues used fluorescent tubulin to identify microtubule morphology and behavior in the growth cone both in vitro in *Xenopus* neural tube cultures and in vivo in grasshopper *Ti1* neurons (Sabry et al., 1991; Tanaka and Kirschner, 1991; Tanaka et al., 1995; Tanaka and Kirschner, 1995). Microtubules were found deep in the growth cone periphery throughout the lamellipodia in three archetypal – but not discrete – states: splayed, looped, or bundled (Tanaka and Kirschner, 1991). When branching or turning, microtubules appear oriented in the direction of future growth in advance of actual growth. Before the final step of elongation (“consolidation” in the standard terminology of (Goldberg and Burmeister, 1986)), looped or splayed structures were often straightened into tight bundles. In vivo with *Ti1* axons, microtubules selectively invaded branches where filopodia had contacted guidepost cells and in cases where microtubules invaded multiple filopodia/directions, retention was selective to branches oriented in the correct direction (Sabry et al., 1991). When microtubule dynamics are inhibited using vinblastine, growth cones continue to wander without forward movement, again indicating an important role for microtubules in consolidation (Tanaka et al., 1995).

In a separate work, the same fluorescent tubulin time-lapse observations from *Xenopus* cultures (Tanaka and Kirschner, 1991) were re-analyzed to examine autocorrelations in microtubule assembly and cross-correlations between microtubule and growth cone advance (Odde et al., 1996). Taken separately, both growth cones and microtubules exhibit strong anticorrelation over a ~ 4 minute timescale. That is, growth cone advances tend to be followed by retractions 4 minutes later (and likewise for microtubule advances and retractions). From their analysis, they assert that Katz (1984) was incorrect in modeling growth cone advance as an uncorrelated random walk. This is not a flaw in Katz’s data or analysis but rather due

to a lack of sufficient temporal resolution. Recall that the temporal sampling resolution of Katz’s observations (10 minutes) would be unable to see correlations over smaller timescales; indeed, the autocorrelation function of growth cone position is approximately zero after 8 minutes (sampling growth cone and microtubule position every 10 seconds).

The similarity in the autocorrelation functions of growth cone and microtubule movements suggests that they might have coupled movements: Growth cone dynamics (advance or retraction) tends to lead microtubule dynamics by 0-2 minutes (ie. positive cross-correlation over those lags). In addition, the authors suggest there might be a more complex coupling in the other direction – microtubules leading growth cones – on a smaller time scale (<20 seconds) but there is only a single data point with a small (but significant) correlation to support this idea.

More recent studies of the axon cytoskeleton show that microtubule reorganization also occurs at branch points (Kalil et al., 2000) and substrate borders (Tanaka and Kirschner, 1995; Williamson et al., 1996). F-actin (predominantly found in filopodia and lamellipodia of the growth cone) and microtubules (predominantly found in the axon shaft) are likely connected to and influence each other (Dent and Kalil, 2001). For example, drugs that affect either cytoskeletal component (eg. by influencing dynamics or polymerization) tend to also affect the other component. There is also still some controversy surrounding the distribution of actin in the axon shaft: whether it is punctuate (Dent et al., 2003) or bundled similarly to microtubules (Bearer and Reese, 1999).

1.2.4 Fluorescence microscopy 2: Labeling synapses with fusion proteins and mammalian neocortex in vivo

In recent years, synaptic fusion proteins have been used to describe the behaviors of the developing axons in terms of synaptic contacts made by those axons. Physical contact between axons and dendrites leads to stabilization of previously mobile VAMP/synaptobrevin-GFP transport packets (Ahmari et al., 2000). In both zebrafish and *Xenopus* optic tectum, accumulation of synaptophysin-GFP puncta leads to stabilization of new axonal branches (Meyer and Smith, 2006; Ruthazer et al., 2006). Smith and colleagues found that in zebrafish tectum the majority of both axonal branches and synaptophysin-GFP puncta are short-lived and, as seen by Cline and colleagues, the lifetimes of puncta (and hence the branches they inhabit) are correlated with their intensity.

Two-photon microscopy in vivo in *Thy1*-GFP mice has shown intrinsic growth differences in local cortical and thalamic axons innervating the same area (Portera-Cailliau et al., 2005). In this particular *Thy1* mouse line, subpopulations of cells express GFP cytoplasmically, including a subset of thalamocortical projection neurons and some Cajal-Retzius local interneurons in layer 1. These two types of neurons grow axonal arbors into overlapping regions in layer 1 of neocortex, yet there are many differences in their axonal growth: different growth cones shapes; different characteristic growth path shapes; different styles of interstitial branching; different methods of branch retraction. This suggests a strong influence of intrinsic factors since the extrinsic environment is the same (layer 1 neocortex) for both types of neurons.

1.2.5 Chemoreception models of axon dynamics

Although space constraints do not permit a review of the experimental literature of molecular guidance cues, the majority of axon growth modeling efforts have focused on modeling responses to these cues. From a simple model with only a few diffusible chemoreceptive signals and no contact interactions, axon fasciculation, outgrowth, and defasciculation at the target can all be reproduced *in silico* (Hentschel and van Ooyen, 1999). When the model is expanded to include random noise (exploratory movement), pathfinding axons – the pioneer axons who first reach a target and provide a path for subsequent axons to follow – emerged from the dynamics (rather than as a special, genetically-specified subclass of axons). Given another model with only contact attraction/repulsion between axons, the same authors conclude that a diffusible, axon-derived chemorepellant is necessary for defasciculation, since contact repulsion from other axons is not sufficient. However, defasciculation could also be achieved via a gradient of attraction and repulsion across a target region, as found in the retinotectal projection (Sperry, 1963; Cheng et al., 1995); the authors did not consider any target-derived chemorepellants in these models. A more sophisticated version of the model (Krottje and van Ooyen, 2007) can handle obstacles in the environment and, as has been mentioned earlier, the intrinsic growth dynamics of axons (Katz and George, 1985; Montague and Friedlander, 1989; Ming et al., 2002; Portera-Cailliau et al., 2005).

Theoretical analysis of guidance cue gradients suggests that growth cones likely use a spatial (versus temporal) gradient sensing mechanism since they move relatively slowly and that gradient steepness must be within a tightly prescribed range, especially for guidance over long distances (Goodhill, 1997; Goodhill and Urbach, 1999). Both gradients and intrinsic growth patterns can provide the impetus for deterministic motion. But what about stochastic motion? Stochastic motion and deterministic motion must be balanced; a growth cone must be able to move stochastically the same amount as it can move deterministically in order to both properly react to guidance cues and to avoid purely random wandering (Maskery et al., 2004; Maskery and Shinbrot, 2005). Of note, these theoretical analyses disagree (and point to supporting experimental data) on what is the right sampling interval for growth cones to “read out” the environment: 6 seconds (Maskery and Shinbrot, 2005) or 60-100 seconds (Goodhill and Urbach, 1999).

Although their use in axon outgrowth is unorthodox, hidden Markov models (HMMs) have found application in diverse fields, including speech recognition (Rabiner, 1989; Jelinek, 1997), protein secondary structure prediction (Sonnhammer et al., 1998; Krogh et al., 2001; Hamelryck et al., 2006), and neural readout of behavioral states (Radons et al., 1994; Abeles et al., 1995). An HMM models a Markov process where the model states are not visible. By observing variables influenced by the model states, the goal is to reconstruct the probabilities of inhabiting and transitioning between model states and the probabilities of the observables given a particular model state. In addition to providing a probabilistic dynamic model, HMMs can segment data into states that have natural interpretations and correspond to real-world phenomena, such as motor behaviors (Abeles et al., 1995) or visual stimuli (Radons et al., 1994) from multielectrode recordings. Aside from biological interpretations, the learnable probabilistic dynamics of axons could be used to automate screening procedures for neurite outgrowth defects (eg. in genome-wide RNAi screens (Schmitz et al., 2007; Sepp et al., 2008)).

1.2.6 Summary

Early time-lapse observations of growth cone and axon behaviors using VEC-DIC led to a description of a stereotyped series of events relating the motions of filopodia, lamellipodia, and the axon shaft to axonal elongation. Newer microscopy technologies such as fluorescent labeling added the dynamics of cytoskeletal components (primarily actin and tubulin) to that description. Recent models of growing axons have focused primarily on responses to external guidance cues, despite the abundance of evidence that intrinsic properties of neurons can greatly influence axonal growth. Very few efforts have been made to model these intrinsic properties: In these models, axon growth over short timescales is well fit by a 1D random walk along the principle direction of elongation. The confluence of new fluorescence microscopy technologies and the re-emergence of intrinsic axon dynamics makes this an apt time for using stochastic techniques to create better, more quantitative models of axon growth.

1.3 Towards a quantitative framework for axon elongation

As nervous systems wire up during development, axon growth cones perform fantastic feats of navigation, traveling enormous distances relative to their size to find their targets. During this process, growth cones exhibit a variety of behaviors, including advancing, retreating, turning, branching, and fasciculation (Sperry, 1963; Heacock and Agranoff, 1977; Risling et al., 1984; Goldberg and Burmeister, 1986; Nakamura and O’Leary, 1989; O’Connor et al., 1990; O’Rourke and Fraser, 1990; Tanaka and Kirschner, 1991; Sabry et al., 1991; Williamson et al., 1996; Kalil, 1996; Szebenyi et al., 1998; Dent and Kalil, 2001; Thomson and Morris, 2002; Tang et al., 2003; Portera-Cailliau et al., 2005; Ruthazer et al., 2006), which have mostly been described in qualitative terms. This paper introduces a mathematical model of the motions of growth cones based on detailed measurements of their dynamical trajectories *in vitro*. As a member of the class of hidden Markov models, our model is statistical and phenomenological rather than mechanistic. It neither invokes mechanical properties such as tension (Bray, 1979; Van Essen, 1997; Shefi et al., 2004) or molecular events such as receptor binding (Goodhill, 1997; Goodhill and Urbach, 1999; Krottje and van Ooyen, 2007; de Gennes, 2007), but it could suggest interesting questions about such mechanisms. Furthermore, fitting our model to data could provide sensitive assays that quantify the effects of manipulations used in mechanistic studies. Such quantitative assays could also be applied to high-throughput screening.

Our work revives an old tradition of studying growth cone motions in cultures of dissociated neurons, dating back to the 1970s and 80s (Bray, 1973; Katz et al., 1984; Katz, 1985b). We have added several innovations made possible by technical advances since then. Our dissociated cultures are of mammalian cortical neurons, rather than the chick, *Xenopus*, or rat sympathetic neurons used previously (Bray and Chapman, 1985; Katz, 1985b; Tanaka et al., 1995; Ming et al., 2002). With time-lapse mosaic imaging of fluorescently labeled neurons, we can examine growth cone movements over longer times (up to weeks) and greater distances. Finally, our fully two-dimensional methods of probabilistic modeling enable a more rigorous quantitative analysis.

We find that growth cone movements exhibit considerable randomness over short time scales, but trajectories are fairly straight over medium time scales (hours), as was previously observed (Bray, 1973; Katz, 1985b). We model this behavior as a two-dimensional biased random walk, which improves upon the one dimensional random walk model that Katz applied to a projection of the growth cone trajectory. The size of the fluctuations in the velocity relative to its mean quantifies the straightness of the growth cone trajectory, a more direct measure than Katz’s fractal dimension. We have also rigorously tested the random walk model by searching for temporal correlations in growth cone velocity.

Straight growth could be relevant for neurons *in vivo*. Static images of some types of neurons show markedly straight axons (Caudy and Bentley, 1986; Sandmann et al., 1996; Braitenberg and Schüz, 1998). Such static images cannot establish whether the initial outgrowth of axons is straight, or whether axons straighten after outgrowth. Our time lapse images suggest that the first hypothesis is true, though they do not rule out the possibility that the second is also true. The functional significance of axon straightness is not known, but it may help maximize contact with as many distinct postsynaptic targets as possible (Stepanyants et al., 2004) and minimize conduction delays (Wen and Chklovskii, 2005).

When observed over longer time scales, our growth cones also appear to occasionally make sharp turns. Therefore we added a model of turning to the biased random walk. The probability of a turn, defined as a change in the direction of the bias, is assumed to be a function of the turning angle. After fitting the model parameters to the growth cone trajectories, we find that the most likely turning angle is about 20 degrees. The biased random walk with turning is a special case of a hidden Markov model, so the fits to data are performed using this probabilistic modeling formalism.

Growth cone turning has been the subject of intense interest in recent years. A great deal of experimental (Lohof et al., 1992; Ming et al., 1997; Shim et al., 2009) and theoretical (Goodhill, 1998; Goodhill and Urbach, 1999) research has revolved around the idea that axons turn when they sense chemical gradients of guidance molecules, either bound to the substrate or diffusing freely. To test this idea, many experiments used ingenious means to create chemical gradients *in vitro* (Walter et al., 1987; Lohof et al., 1992; Rosoff et al., 2004). In contrast, we have imposed no chemical gradients on our cultures. Of course, this does not exclude the possibility that endogenous gradients or other external cues exist in our cultures. Each of our fluorescently labeled neurons is surrounded by other labeled neurons and an even larger number of unlabeled neurons and glia.¹ Therefore our observed growth cone behaviors could be influenced by molecules secreted by other cells into the culture medium, or molecules bound to the surface of other cells. For this reason, interpreting whether our observed growth cone behaviors are the result of an autonomous program or a response to external cues is somewhat speculative, and will be taken up in the Discussion.

¹Previous time lapse studies employed phase-contrast imaging to follow individual axons in very low density (or single neuron) cultures of chick, *Xenopus*, or rat sympathetic neurons (Bray, 1970, 1973; Katz et al., 1984; Katz, 1985b,a). The observed behaviors were interpreted as being intrinsic to the axon, as it was isolated from external influences. We did not attempt to culture cortical neurons in complete isolation from other cells because this is very difficult under the best conditions, even with glia-conditioned medium (Banker and Goslin, 1998), and probably impossible in our time-lapse experiments. The closest possibility would be to culture a single cortical neuron on a carpet of astrocytes, but this would not eliminate interactions with other cells.

Chapter 2

Long-term fully-automated time-lapse of growing axons for weeks

To visualize growing axons, we created dense cultures of a mixture of EGFP-expressing and wild-type primary mouse cortical neurons. In these mixture cultures, only 5-10% of plated cells came from EGFP mice and therefore the axonal growth cones of these neurons could easily be followed under fluorescence observation. This sparse *fluorescent* labeling is necessary: Previous time-lapse studies have employed phase-contrast imaging, where individual axons can be followed only in very low density (or single neuron) cultures (Bray, 1970, 1973; Katz et al., 1984; Katz, 1985b,a). However, mammalian cortical neurons fail to survive for longer periods of time in isolation, even when cultured in glia-conditioned media. Rather, they must be plated at higher densities with neighboring cells. At higher densities, individual axons are impossible to follow with phase-contrast (or DIC) imaging and hence require a sparse fluorescent labeling of individual neurons. Others have used lipophilic dyes and fluorescent protein transfection to similarly achieve sparse labeling. The mixture culture labeling is brightly fluorescent from the earliest stages of axon outgrowth and has none of the toxicity associated with transfection or infection. Figure 1A shows a single time point of the mixture culture in both brightfield (showing all cells) and GFP (showing only 5-10% of the cells) channels.

Using an automated stage, we were able to image multiple axons inside an approximately 1 mm² area on the dish. Cultures were imaged with an incubated microscope for 5 day periods between DIV2 through DIV14. Throughout this time period, axons elongate as the 10-20 μ m growth cones on their distal tips move through the culture. Most data came from axons between DIV5 and DIV10, a period during which functional synaptic transmission is known to begin in rodent hippocampal cultures (Renger et al., 2001). Although the filopodia of the growth cone are highly motile structures, translocation of the entire growth cone is difficult to see in real-time and occurs on a timescale of minutes. Time-lapse imaging is necessary to see growth cone movement, which consists primarily of elongation, retraction, and pausing (see Supplementary Movie). Images of the entire 1 mm² area were acquired every 10 minutes. By imaging continuously for days at 10 minute intervals, we are able to examine the growth cone's movement behaviors on both shorter and longer timescales.

2.1 Primary cortical neuron mixture culture

Sparse cultures of 10% EGFP-expressing cortical neurons were created by mixing dissociated neurons from EGFP mice (Okabe et al., 1997) with wild-type littermates. EGFP mice were generated by breeding EGFP^{+/-} males with WT females. EGFP expression is under the control of the chicken beta-actin promoter and cytomegalovirus enhancer; hemizygous mice express EGFP brightly in almost every cell, starting from the 4 cell stage (Okabe et al., 1997). Unlike other non-mixing techniques such as lipofection, electroporation, biolistics and virally-mediated gene transfer, the mixing system expresses fluorescent protein from the earliest stages of axon outgrowth and does not have added toxicity from gene delivery which is known to be problematic for primary neurons.

Cells from EGFP and WT P0-2 mouse neurons were obtained using a protocol similar to one described elsewhere (Banker and Goslin, 1998; Sanjana and Fuller, 2004). EGFP and WT tissues were dissociated simultaneously but separately until the final, pre-plating mixing step. The dissection solution was HBSS (Sigma H2387) supplemented with 4mM NaHCO₃ and 5mM HEPES. Cortical tissues were proteolyzed for 40 min at 37°C, followed by rinsing and trituration in the plating medium. The digestion solution consisted of dissection solution plus 20U/mL papain (Worthington 3126), 0.5mM EDTA, 1.5mM CaCl₂, 1mM L-cysteine, and 1µg/ml DNase I (Sigma D5025). The plating medium consisted of serum-free Neurobasal A without phenol red, (Gibco/Invitrogen 12349015) with 2% B27 and 2mM Glutamax (Brewer et al., 1993). After trituration with a fire-polished tip, EGFP and WT suspensions were counted with a hemacytometer and mixed such that the final suspension had 5-10% EGFP cells. This suspension was centrifuged to remove debris and resuspended at a density of 200K/mL. The mixture culture was then plated on an existing monolayer of astrocytes in 35mm glass-bottom, black wall petri dish (World Precision Instruments Fluorodish FD35B-100). Astroglia monolayer cultures are commonly used to provide trophic support for cultured central nervous system neurons (Kaeche and Banker, 2006). Astroglia were cultured from dissociated P0 Sprague-Dawley rat cortical cells plated at low density (10K/mL) in serum-containing medium. After 1 week in vitro, astroglia cultures were left overnight on an orbital shaker to eliminate any remaining neurons, trypsinized, and re-plated into the Fluorodishes at 20-50K/mL density. Neurons are plated on top of these astroglia after they reach confluence, which normally occurs in 1 to 2 weeks after glia plating. Feeding of the EGFP mixture culture was done with the same serum-free medium (50% replacement every 4 days in vitro).

2.2 Time-lapse imaging

We monitored axonal growth using a custom, incubated widefield fluorescence microscope. Images of an approximately 1 mm² area were captured every 10 minutes continuously over periods of 5-14 days usually from DIV5 onwards. Our imaging platform was built around an Olympus IX71 inverted microscope using a 60x/NA0.7 or 40x/NA0.75 objective for each experiment. Individual images were captured using a cooled CCD camera (Roper Scientific CoolSnap HQ) with an effective pixel width of either 0.323µm (with 60x objective) or 0.147µm (40x) and later montaged together (5x5 individual tiles) to cover a large area.

Images were captured with approximately 100 pixels of overlap in each direction to ensure accurate montaging. For the tiling and autofocus, the sample was attached with a custom mount to a 3D computer-controlled manipulator (Sutter Instruments MP-285). We used a fiber-coupled 625 mW blue (470 nm) LED (ThorLabs MBLED) for fluorescence illumination with hard-coated GFP filters (Semrock BrightLine GFP-3035B). Along with each GFP image, we captured a phase (60x) or standard brightfield (40x) image.

Due to the long duration of our experiments (up to weeks) and despite stable temperature control over a large volume (see below), it was necessary to have an accurate autofocus routine to refocus the sample when appropriate. Our goal was to build an autofocus system that would require minimal time - to avoid spending too much time on a single tile, given the many tiles in the montage - and minimal blue light exposure to the sample since blue light phototoxicity is a problem for biological preparations (Hockberger et al., 1999; Hockberger, 2002).

Autofocusing was performed using phase/brightfield images for every tile at every time point using a simple local search. For the local search, we took 3 phase/brightfield pictures. Because of the small number of focal planes, autofocusing on each tile was very fast (~ 1 sec). One picture was taken at the focus for that tile from the previous time point and two more at a fixed distance above and below the focus. This fixed distance was empirically determined by examining a range of values between 0.2 μm and 5 μm ; for most experiments, we used a distance of 0.8 μm . Very small values resulted in an oscillating focal plane and very large values could not react quickly enough to slow gradual drifts, which was our most common focus issue. Additionally, for the first image, a more extensive autofocus routine was used to search over a larger range of values to find the best initial focus. In this case, each tile was seeded with the best focus from a neighboring tile and then pictures were taken 3 μm above and below that focus in 1 μm increments. Focus was evaluated by filtering each image with a 2D Laplacian ($\sigma = 1.5$, kernel size=10 pixels), squaring, and then summing over all pixels (Price and Gough, 1994). The best focus was chosen as the z position where the corresponding phase/brightfield image maximized this quantity. The GFP image was taken at the same focus, thus allowing us to refocus the sample at every time point without any additional blue light exposure.

Control of the microscope, camera, external shutters, and 3D stage were automated using custom programs written in C and MatLab (The MathWorks, Inc.). The entire microscope was incubated using a large transparent plastic enclosure (Solent Scientific Ltd.) to ensure temperature stability with a smaller custom container over the sample into which we continuously injected a humidified 5% CO₂/10% O₂/85% nitrogen artificial atmosphere (Airgas Z03NI8532000113). The microscope enclosure was heated to 36°C by a convection heater placed in one corner and controlled with a feedback sensor placed near the sample (Solent). The artificial atmosphere was first warmed by running the gas through the included tubing coil inside the heated enclosure and then humidified by bubbling it through a water chamber placed directly over the heating element. The exit tubing from the water chamber to the sample container was kept to a minimum and arranged such that the direction of humidified gas flow was always from higher to lower temperature regions. This ensured that minimal humidity loss via condensation would occur before the gas reached the sample container. The sample container was built using a thick wall aluminum frame (ThorLabs LCP01) with a luer port for gas input on the side and a cut 0.062" thickness polycarbonate transparent

window (McMaster-Carr 8574K24) sealed with TorrSeal (Varian) on top.

2.3 Image alignment and growth cone tracking

Our initial task was to stitch together individual tiled images (taken with overlap) into a single large montage image for each timepoint. Given that the 3D stage has submicron resolution and very low drift, we found that the alignment of neighboring tiles between timepoints changed very little over the course of a single experiment but that re-alignment was necessary between different experiments. So, for each experiment, phase/brightfield images from a single timepoint were aligned initially in Photoshop (Adobe Systems) manually and then the same alignment was applied to stitch together all other timepoints for both phase/brightfield and GFP channels.

Our next goal was to extract the positions of individual growth cones over time from the image stacks. Axons were identified as thin, long and non-tapering cell processes. Tracked axons had very few branching events (as expected, see Katz (1985b)) and most of those branches were transient; in all cases of branching, the larger or longer branch was followed and the other branch ignored. For each axon, we identified and recorded the x - y position of the GFP-rich growth cone in each frame where the growth cone was present. The center of the growth cone was located using a custom MatLab GUI to display a 300% magnified view of a subregion of the montage around the growth cone. All subsequent analysis is done only on the growth cone positions $\vec{r}(t) = (x(t), y(t))$ at each time t .

To ensure accurate labeling of growth cone centers, a subset of the data ($n = 202$ frames) was labeled by a second human tracer. The average Euclidean error between the two labelings was $1.1 \pm 0.2 \mu\text{m}$. which is less than the average step size ($6.9 \pm 0.1 \mu\text{m}$) or the standard deviation for the fitted random walk models.

Chapter 3

Quantitative analysis of axon elongation: Steps and stochastic models

3.1 Time series of velocity vectors

We manually digitized the trajectory of the growth cone, yielding a time series of position vectors $\vec{r}(t) = (x(t), y(t))$ sampled at 10 minute intervals (see Methods and Figure 1B). We will refer to the difference between successive pairs of position vectors,

$$\vec{v}(t) = \vec{r}(t) - \vec{r}(t - 1)$$

as the *velocity* of the growth cone (see Figure 1C). Here velocity has the same units as position, as time is measured in units of the sampling interval. It can be converted to more standard units by measuring time in minutes or hours.

For illustrative purposes, some of the analyses below were applied to single axon trajectories, or segments of trajectories. But most reported results are population averages over 8 axons from 3 separate cultures ($n = 1440$ growth cone positions). Unless otherwise indicated, numerical results are presented as mean \pm standard error.

We defined the average speed of an axon as the time average of $|\vec{v}(t)|$. The population average of this time-averaged speed was 44.7 ± 4.0 $\mu\text{m/hr}$. The axons were tracked over an average time of 30.4 hours (range 15.2 to 59 hours).

3.2 Mean and covariance of the velocity

For pedagogical purposes, our analysis will initially be confined to a single growth cone trajectory, that of the axon shown in Figure 1B and C. The red points in Figure 2A depict a 11-hour long (66 samples) growth cone trajectory of the same axon. The velocity vectors from this trajectory are plotted in Figure 2B. Their mean is nonzero, reflecting that the movements of the growth cone have a systematic bias. We will call the mean velocity the *bias vector* \vec{b} , or simply the *bias*. This quantity will play an important role in what follows.

It will prove convenient to decompose each velocity into components that are parallel

and perpendicular to the bias,

$$\vec{v} = \vec{v}_{\parallel} + \vec{v}_{\perp}$$

Figure 2B shows this decomposition in schematic form for one velocity. The mean of \vec{v}_{\parallel} is equal to \vec{b} , while the mean of \vec{v}_{\perp} vanishes.

To quantify the fluctuations in the velocity, we computed the covariance matrix C . As shown by the ellipses in Figure 2D, the principal eigenvector of the covariance matrix points almost exactly in the direction of the bias \vec{b} . Since the angular difference in the directions is so small ($\sim 1^\circ$) we will regard this difference as zero in the following. More formally, this approximation can be expressed in terms of \bar{C} , the covariance matrix in the coordinate system defined by the directions parallel and perpendicular to the bias. We'll assume that the off-diagonal elements of this matrix vanish,

$$\bar{C} \approx \begin{pmatrix} \sigma_{\parallel}^2 & 0 \\ 0 & \sigma_{\perp}^2 \end{pmatrix} \quad (3.1)$$

The variances σ_{\parallel}^2 and σ_{\perp}^2 quantify the fluctuations in \vec{v}_{\parallel} and \vec{v}_{\perp} , respectively. According to the data, $\sigma_{\parallel}^2 > \sigma_{\perp}^2$, which means that the fluctuations are larger in the parallel direction than in the perpendicular direction. If σ_{\perp} were zero, that would mean that the growth cone moves in a completely straight trajectory. Therefore we defined an index of straightness as the ratio between the magnitude $b = |\vec{b}|$ of the bias and σ_{\perp} ,

$$IS = \frac{b}{\sigma_{\perp}} \quad (3.2)$$

For the red segment in Figure 2A, this index was 1.8.

3.3 Temporal correlations of the velocity

The above analysis considered only the covariance between the components of the velocity vector at equal times. We also quantified temporal correlations in the velocity vectors using the autocorrelogram and the periodogram.

We first considered the parallel component \vec{v}_{\parallel} of the velocity. None of the autocorrelations were significant, either individually (extremum $r = -0.26$ at 3 hours, $p > 0.05$ with Bonferroni correction for tests at 18 lags) or when tested together (Ljung-Box portmanteau test for random residuals, $Q = 20.8$, $p = 0.30$). The normalized periodogram was indistinguishable from that of a white noise process (Bartlett's Kolmogorov-Smirnov test, $p = 0.31$) and exhibited no significant single periodicities (Fisher's exact g , $p(g \geq g^*) = 0.44$). Plots can be found in supplemental figure XX.

Then we considered the perpendicular component \vec{v}_{\perp} of the velocity. Although some periodicity the autocorrelogram seems evident to the eye (see Supplemental Figure XX), but these correlations are not significant individually (extremum $r = 0.24$ at 20 minutes, $p > 0.05$ with Bonferroni correction for tests at 18 lags) or when tested together (Ljung-Box portmanteau test for random residuals, $Q = 27.5$, $p = 0.07$). The normalized periodogram of \vec{v}_{\perp} is indistinguishable from that of a white noise process (Bartlett's Kolmogorov-Smirnov test, $p = 0.07$), and exhibits no significant single periodicities (Fisher's exact g , $p(g \geq g^*) =$

0.13).

The perpendicular and parallel components of the velocity do not have significant cross-correlation (likelihood ratio test, $r = 0.05$, $p = 1$).

3.4 Biased random walk model

By definition, each step of a random walk is drawn independently from an identical probability distribution. The above tests of independence suggest that the growth cone trajectory can be modeled as a random walk. Since the velocity has a nonzero mean, the random walk is said to be *biased*.

We chose a Gaussian form for the probability distribution of the velocity,

$$g(\vec{v}, \vec{b}, C) \propto \exp\left(-\frac{1}{2}(\vec{v} - \vec{b})^T C^{-1}(\vec{v} - \vec{b})\right) \quad (3.3)$$

(A normalization factor has been omitted from the equation for brevity.) The mean \vec{b} and covariance C were estimated as above from the points in Figure 2C, imposing the constraint (3.1) on C . The ellipses of Figure 2D can be interpreted as equal probability contours of the estimated Gaussian. We generated a random walk from this model, and it looked similar to the real growth cone trajectory (Figure 2E).

This biased random walk (BRW) model is related to one used previously by Katz and colleagues for chick dorsal root ganglion and frog neural tube axons grown *in vitro* (cite). They projected the two-dimensional trajectory onto one dimension, and applied a model of a random walk on a 1D lattice. In contrast, our Gaussian model is two-dimensional, and the index of straightness of Eq. (3.2) is directly based on it. In contrast, Katz and colleagues quantified straightness using the fractal dimension, which is only remotely related to their random walk model.

3.5 Changes in the bias

Is the BRW model applicable over longer time scales? Looking at 11 further hours of growth cone movement from the same axon as before (Figure 2A, blue segment), we see the axon turns and continues in a new direction. Supplementary Figure 1 shows that the velocities from this trajectory have significant temporal correlations in \vec{v}_\perp (Ljung-Box portmanteau test for random residuals, $Q = 76.9$, $p < 10^{-8}$). This means that the independence assumption of the random walk model is violated.

This suggests that we divide the trajectory into two segments, and fit a separate BRW model to each segment. These two random walks have different biases and different covariances. However, if the velocities for each segment are plotted in a coordinate system defined by the directions parallel and perpendicular to the bias for that segment, then the distributions appear similar. This suggests not only that the approximation (3.1) holds, but also that the variances are similar in both segments. In this coordinate system oriented by the bias, it turns out that the velocities from the two segments are statistically indistinguishable (Hotelling's T^2 -test: $T^2 = 3.14$, $p = 0.21$; Levene's test for equality of variances: $T^2 = 0.23$,

$p = 0.88$). Within each segment, statistical independence of the velocities holds (data not shown).

In summary, over short timescales (i.e. hours) the BRW model works well. Over longer time scales, the independence assumption is violated because the direction of the bias changes. This suggests that we can improve the BRW model by augmenting it with a model of how the bias vector changes over time.

3.6 Hidden Markov model

We assume that the time series of bias vectors $\vec{b}(t)$ is of the form

$$\vec{b}(t) = b \left(\cos \frac{2\pi i(t)}{n}, \sin \frac{2\pi i(t)}{n} \right)$$

where $i(t)$ can take on the values 1 through n , and the magnitude b is assumed constant in time. This form discretizes the angle

$$\theta(t) = \frac{2\pi i(t)}{n}$$

of the bias vector so that its possible values are evenly spaced on the circumference of a circle. Note that the time series of bias vectors $\vec{b}(t)$ is equivalent to the time series of natural numbers $i(t)$.

At each time step, the probability of the transition $i(t-1) \rightarrow i(t)$ is given by

$$f(i(t) - i(t-1))$$

where the function f is assumed periodic with period n . The dependence on the difference $i(t) - i(t-1)$ enforces rotational symmetry, so that the probability of a transition depends only on the angular difference between successive bias vectors. Rotational symmetry is a reasonable assumption, as there is no reason why any direction should be special in the dissociated culture. Note that f has the properties of a probability distribution, i.e., its values are nonnegative and satisfy the constraints $\sum_{i=1}^n f(i) = 1$. Therefore it is specified by a total of $n-1$ parameters. A schematic of the hidden states and their transitions is shown in Figure 3.

Now that we have a model of the dynamics of the bias vectors, we can combine it with the BRW model. Simply assume that the velocities are drawn from a BRW with a bias vector that changes dynamically according to the above. More precisely, the velocity $\vec{v}(t)$ at time t is generated by drawing from a Gaussian distribution with mean $\vec{b}(t)$ and covariance $C(t)$, as in Eq. (3.3).

As explained earlier, the covariance matrix is assumed to have the diagonal form \bar{C} of Eq. (3.1) in the coordinate system defined by the bias. More explicitly, this means that

$$C(t) = R(t)\bar{C}R(t)^T$$

where

$$R(t) = \begin{pmatrix} \cos \theta(t) & -\sin \theta(t) \\ \sin \theta(t) & \cos \theta(t) \end{pmatrix}$$

is the rotation matrix defined by the angle of the bias vector. In summary, the adjustable parameters of the model are the bias direction transition function f , the magnitude b of the bias vector, and the variances σ_{\parallel}^2 and σ_{\perp}^2 , for a total of $n + 2$ parameters.

This is a special case of a hidden Markov model (HMM), a general formalism for modeling a sequence of observations using a hidden state variable generated by a Markov process (cite). The hidden state in the model is the bias vector $\vec{b}(t)$, and the observations are the velocity vectors $\vec{v}(t)$. HMMs have been widely applied in automatic speech recognition, bioinformatics, neurophysiology, and many other problem domains (cite). The function f specifies the transition probabilities of the hidden state, and the Gaussian distribution specifies the *emission probabilities* of the observations given the hidden state. In our problem, we have a prior expectation of rotational symmetry, and that is used to constrain both the transition probabilities and the emission probabilities.

3.7 Automatic segmentation and parameter learning

Given a time series of velocities, and an HMM, we can segment a trajectory by finding the sequence of hidden states $i(t)$ that maximizes the likelihood of observing the velocities.

$$L = \prod_t f(i(t) - i(t-1))g(\vec{v}(t), \vec{b}(t), C(t))$$

This optimization can be performed efficiently and exactly using the Viterbi algorithm. (citation? should we cite both the original Viterbi paper and the super-cited Rabiner tutorial?). The procedure is sometimes called inference, because the hidden states are not directly known, but must be inferred using the model from the time series of observations.

While the Viterbi algorithm gives the best segmentation given an HMM, the result will be useless unless the HMM is a good model. Therefore it is important to fit the parameters of the HMM to the data. This can also be done by the method of maximum likelihood. In Viterbi learning, the likelihood L is jointly maximized with respect to the hidden state sequence and the parameters of the model. This is done iteratively by alternating between a segmentation step and a parameter adjustment step. The likelihood is guaranteed to be nondecreasing under both of these steps.

3.8 Results of the HMM

Viterbi learning (see Stochastic modeling in Methods) was run until convergence of model parameters, which usually occurred after a few iterations. All HMMs were fit to data from the complete trajectories of 8 axons. From now on, all results are reported for populations of growth cones, unlike the BRW results above, which were illustrated for small segments of a single growth cone trajectory for pedagogical purposes.

Figure 4 depicts the results from a model with $n = 36$ hidden states. Figure 4B shows an example of the emission probability distribution after convergence, in the coordinate system defined by the bias of the hidden state. This looks much the same as the distributions that were derived from fitting the BRW model to segments of the trajectory that were chosen by hand. The difference here is that the segments of the trajectory are produced automatically by the HMM. Figure 4A (third column) shows example HMM segmentations for 4 different axons. The HMM segmentations seem to correspond to how a human might divide a growth cone trajectory into straight segments.

The learned transition probabilities are shown in Figure 4C. The quantity $f(0) = 0.96$ is the probability that the bias vector stays the same. This quantity is close to one, so no change in bias is by far the most likely behavior. From this we can calculate the mean persistence time in a single hidden state as

$$t_{\text{persistence}} = \frac{1}{1 - f(0)} = 283 \text{ minutes}$$

Thus the growth cone tends to move in the same direction for about 4 hours before turning.

While the growth cone tends to move straight, every now and then it turns. In Figure 4C, the second largest transition probability is for a turn of 40° . Small angle turns have zero probability. Therefore in the HMM found by Viterbi learning, turns are sudden rather than gradual.

Large angle turns ($>70^\circ$) also have low probability in the HMM. This may seem inconsistent with the fact that large branching angles can be observed in static images of fixed neurons (Thanos and Bonhoeffer, 1987; Risling et al., 1984; Myers et al., 1986; Imondi and Kaprielian, 2001). But our result is consistent with time-lapse studies of cortical axons *in vivo*, which have remarked specifically about *not* observing large angle turns of the growth cone, even when the final configuration of the axon exhibits large angle bends (Halloran and Kalil, 1994; Portera-Cailliau et al., 2005). According to one resolution of this seeming inconsistency, the large angle bends are not created by growth cone turning, but instead by retraction of one branch of a large angle branching. (O’Leary et al., 1990; Szebenyi et al., 1998; Kalil et al., 2000; Dent et al., 2003; Nakamura and O’Leary, 1989). Note that the branching of cortical axons appears to be interstitial, i.e., branches grow out from locations behind the growth cones. Therefore our growth cone observations did not include branching events.

3.9 Validating the model

Viterbi learning can become trapped at local maxima of the likelihood. The learned transition probabilities were robust to different random initialization labeling (data not shown) and to different training data as assessed by leave-one-out cross-validation (Figure 4C, right). Even starting from significantly different initial conditions, the final segmentation and model parameters were similar. Similarly, the emission probabilities were also robust (different initial conditions: $V_{\parallel} = 4.96 \pm 0.02 \text{ } \mu\text{ms/sample}$, $V_{\perp} = 0.07 \pm 0.13 \text{ } \mu\text{ms/sample}$; leave-one-out cross-validation: $V_{\parallel} = 5.00 \pm 0.12 \text{ } \mu\text{ms/sample}$, $V_{\perp} = 0.02 \pm 0.03 \text{ } \mu\text{ms/sample}$).

Do the HMM-produced segments fulfill the conditions of a BRW? Again we apply the

tests of temporal independence. To do this, we rotated the steps from each segment into a unified coordinate system (as defined by the segment’s hidden state direction), and calculated frequency-domain periodograms and time-domain correlograms for each segment. Supplementary Figure 2 shows the cumulative normalized periodograms, averaged over all segments. In the direction perpendicular to elongation, there is hardly any deviation from the random walk (white noise) steps (Bartlett’s Kolmogorov-Smirnov test, $p = 0.99$). In the parallel direction, there is a barely significant deviation at lower frequencies (Bartlett’s Kolmogorov-Smirnov test, $p = 0.04$), indicating that some segments might have a different elongation speed between beginning and end of the segment. No single significant periodicities were detected along either direction (Fisher’s exact test $p(g \geq g^*) = 0.85, 0.99$ for parallel and perpendicular directions, respectively). Time domain analysis produced similar results (see Supplementary Figure 2).

The “hole” in the transition probabilities at small angles suggests that the growth cone tends to turn suddenly rather than gradually. However, it is not clear whether this is truly a property of the data, or simply an artifact of our choice of model. Perhaps the model would impose this sort of transition probabilities on any kind of trajectory. To test this possibility, we generated artificial trajectories that curve gently. A sine-generated curve has been used to model meandering rivers (Langbein and Leopold, 1966) and flagellar motion (Hiramoto and Baba, 1978). For such a curve (Figure 5A), the angle of the velocity vectors changes as a sine function: $v_{\Theta}(t) \propto \sin(2\pi t)$. The same HMM framework trained on sine-generated curves (with additive and multiplicative Gaussian noise) results in transition probabilities that are nonzero only for small angles (Figure 5B). Segmentations of the sine-generated curve from this HMM reflect this: Over the course of a turn, transitions are made between several adjacent hidden states .

Another possibility is that the discretization of the hidden state could introduce artifacts in the modeling. Above we allowed the bias vector to take $n = 36$ angles. We also trained an HMM with 10 times as many hidden states ($n = 360$) with Viterbi learning. In this HMM, there is a separate hidden state (heading) for every 1° along the unit circle. As seen in Supplementary Figure 3, the transition probabilities, emission probabilities and resulting segmentations from the 360 state model are similar to those of the 36 state model.

3.10 Bias versus persistence

What is the biological basis of the bias of the random walk? Does it come from an external cue, such as a chemical gradient? This seems unlikely for several reasons. First, the dissociated culture does not have any obvious orientation, unlike a brain slice or an intact brain. Second, the growth cones move in all directions in the culture, so that there would have to be many different external cues, one for each direction of motion. Third, the growth cones switch directions every now and then, so that they would have to switch external cues.

Another interpretation is that the axon has a “memory” of its direction, that it executes an intrinsic program to continue moving in whatever direction it has been moving before. According to this idea, the motion of the growth cone is *persistent* rather than biased. To explore this possibility, we fit an autoregressive (AR) model to our data, in which the next velocity is generated by adding noise to a linear combination of the T previous velocities

$$\vec{v}(t) \approx \sum_{\tau=1}^T c(\tau) \vec{v}(t - \tau)$$

Note that the parameters of this model contain no direction, unlike the BRW model. Instead, directionality of a trajectory arises from the initial conditions of the velocity time series.

3.11 Retractions

Shorter segments seem to be found in decision areas (see closeup in Figure 10B), where the axon growth cone might "try out" a growth direction, retract, and continue in another growth direction. Out of all the segments, slightly less than half of them (46%) are shorter than 50 μ m. To test if retractions are often found near shorter segments, we computed the mean direction of movement within each segment and the angle between the mean directions of neighboring segments. Figure 6C shows a plot of the angle at the boundary between segments versus the length of the subsequent segment. Segments where the boundary angle was less than 90° had a mean segment length of 114 \pm 19 μ m and 37% of them were shorter than 50 μ m. Segments where the boundary angle was greater than 90° (ie. backwards movement) had a mean segment length of 22 \pm 8 μ m and 90% of them were shorter than 50 μ m. These short segments following large angle changes point to a deficit in the model: The HMM is not capturing such retractions in the emission probabilities and thus resorts to hidden state changes to account for the retractions.

3.12 Stochastic modeling methods

Custom MATLAB code was used for all hidden Markov model simulations.

Although different algorithms are available for HMM training, we use the Viterbi learning procedure, which maximizes the joint probability of the observations and model states $p(V, H)$ (Juang and Rabiner, 1990). Briefly, unsupervised learning of model parameters from the data consists of alternating maximum likelihood updates of transition and emission probabilities and of the hidden states sequence for each growth cone trajectory.

Unlike the discrete hidden state transitions, we need to fit a continuous distribution for the emission probabilities since the velocities themselves are continuous. It is reasonable to fit a normal (Gaussian) distribution, since we expect that there is some (unknown) spread of observed velocities around a (unknown) mean velocity for each state. The learning procedure requires initial guesses for hidden state transition and emission probabilities and, as shown below, is robust to different initializations. Random initialization of HMM parameters is done as follows: For each axon, the velocity vector observations are divided randomly into segments (sampled from a uniform distribution with a maximum segment length of 20). Initial transition and emission probabilities are estimated directly from this labeling. The initial assignment of segments to hidden states is done by calculating, for each segment, the direction of mean velocity vector. The segment is assigned to the hidden state whose direction was nearest to the direction of the mean velocity vector.

From these assignments, maximum likelihood initial transition and emission probabilities are calculated to begin Viterbi learning. Inherently, the Viterbi learning procedure cannot increase the probability of any transition that has previously been assigned zero probability. To prevent the initialization of transition probabilities (based on the random segmentations) from unnecessarily constraining the search space, transition probabilities are amended after initialization but before learning such that all transitions have a probability equivalent to at least 3 transitions over the entire data set. In our case, the data set had 1440 possible transition opportunities. For transitions where the maximum likelihood fit to the initial labeling allocated less than this probability, the additional probability needed is taken from the transition for staying in the same hidden state.

3.13 Figures

Time-lapse HMM paper: List of figures

Neville Sanjana and H. Sebastian Seung

November 1, 2009

Figure 1.

- A:** Single field of view from automated montaging time-lapse system taken from a cortical mouse GFP mixture culture at DIV6. The field of view is assembled from 25 individual X-Y tiles and spans 1.00 mm x 0.76 mm. Each full resolution montage image is 29.4 megapixels (6218x4732 pixels at 0.161 μ m/pixel). The brightfield image (left panel) shows all the cells in the field of view. The right panel shows only the GFP-expressing cells in the same field of view. Note that only a small subset of the cells visible in the left panel are GFP-expressing. The neurites of these cells are obscured in the brightfield image but clearly visible in the GFP image. Scale bars: 50 μ m.
- B:** In these GFP images (colors inverted for clarity), the location of a single growth cone's center is marked (black circle) in three (consecutive) images 10 minutes apart and one image 4.5 hours later. Scale bar: 10 μ m.
- C:** Same data as B with the location of the growth cone plotted from each frame (ie. every 10 minutes). Images in B correspond to the second, third, fourth, and last data points in the plot. Velocity vectors (arrows) are drawn with arrowhead sizes scaled by their magnitude.

Figure 2.

- A:** A single axon growth cone's position over a 22 hour period. The change in color (red to blue) at the halfway point (11 hours) is approximately where there is a change in elongation direction.
- B:** Schematic diagram of different velocity vectors. Velocity vectors indicate the direction of elongation between five sequential growth cone positions. A single velocity vector can be decomposed into x - y components (v_x, v_y) or into components parallel and perpendicular to the elongation direction (v_{\parallel}, v_{\perp}). The elongation direction is defined by the line connecting the first and last positions in the trajectory.
- C:** The same growth cone trajectory from A plotted in velocity space. Red points are velocities from the first half of the trajectory and blue points are velocities from the second half as in A.

- D:** Gaussians distributions fitted to velocities from each half of the trajectory. For each distribution, the mean velocity $\bar{\mu}$ is non-zero, reflecting a tendency to move straight. The spread in the direction perpendicular to the mean, σ_{\perp} , can be used to characterize how directed the elongation is.
- E:** Generated trajectory from one distribution. Positions are integrated velocities, which are sampled from the fitted red distribution in D. These positions have a similar elongation path to the red segment in A.
- F:** Velocities from C plotted in a coordinate system defined by the mean velocity $\bar{\mu}$ for each segment. In this coordinate system, the velocities from the two segments are statistically indistinguishable (Hotelling's T^2 -test: $T^2 = 3.14$, $p = 0.21$; Levene's test for equality of variances: $T^2 = 0.23$, $p = 0.88$).

Figure 3. Schematic of hidden Markov model. Blue squares with small black arrows represent hidden states, which are equally spaced around the unit circle. Transitions between two states i and j (a_{ij}) depend only on the relative angle between the two states. State transitions from a single hidden state are indicated by colored dashed arrows. Arrows with the same color (i.e. same angular separation from current state i) have the same probability. For clarity, transitions from the 135° hidden state are the only ones drawn but there are similar transitions for all of the other hidden states and fewer states are shown than in the the actual HMM (36 or 360).

Figure 4.

- A:** Examples of HMM segmentation. The first column shows sequential points from manual tracking of the growth cone position at 10 minute intervals. Initially, each growth cone trajectory is randomly segmented by sampling segment lengths from a uniform distribution. Color changes denote separate segments/ changes in elongation direction. After the HMM parameters have converged, we find the most probable segmentation of each trajectory into different elongation directions (second column)
- B:** Initial (left) and final (right, after convergence of HMM parameters) emission probabilities. The emission probabilities, which characterize the elongation in a particular direction, are parameterized by a 2D gaussian over velocities parallel and perpendicular to the hidden state (elongation direction). After learning, emission probabilities are more oriented along the elongation direction. Distributions shown are the mean distributions from leave-one-out cross-validation for a 36-state HMM trained on the axon growth cone positions.
- C:** Initial (left) and final (right) transition probabilities between hidden states. Transition probabilities are parameterized by the *difference*

in angle between heading directions. Initial transition probabilities reflect the transitions found in the randomly segmented axon growth cone positions; also, before Viterbi learning, all transitions have at least some minimum probability. Transition probability error estimates (error bars are standard error) are from leave-one-out cross-validation for a 36-state HMM trained on the axon growth cone positions.

Figure 5.

- A:** HMM segmentation of sine-generated curve. Instead of growth cone data, positions along a sine-generated curve with noise were used to train an HMM. The trajectory was initialized with a random segmentation generated by sampling segment lengths from a uniform distribution (first column). Color changes denote separate segments/changes in elongation direction. The second column shows the most probable segmentation of the trajectory after the HMM training converges.
- B:** Initial (left) and final (right, after convergence of HMM parameters) transition probabilities between hidden states for a HMM trained on sine-generated curves. Initial transition probabilities reflect the transitions found in the randomly segmented sine-generated curve; also, before Viterbi learning, all transitions have at least some minimum probability. Transition probability error estimates (error bars are standard error) are from different initial segmentations ($n = 10$) for a 36-state HMM trained on the sine-generated curve.

Figure 6.

- A:** Histogram of segment (hidden state) durations from the HMM segmentation of growth cone data. An exponential fit to these durations yields a mean duration of just over 4 hours and is not significantly different than the predicted mean duration from the learned HMM transition probabilities.
- B:** Histogram of the deviation from the hidden state direction for each velocity over all segments. Although most velocities are oriented along the elongation direction, there exists a broad distribution of orientations within segments.
- C:** Distribution of angles at segment boundaries in growth cone data. The ordinate shows the angle between the mean velocity heading 2 hours before and after the segment whose duration is plotted on the abscissa begins. The dotted red line indicates 90° (angles greater than 90° indicate backward motion/retraction). The majority of segments in the region $>90^\circ$ are of shorter duration.

Figure 7.

- A:** Mean residual (error) for autoregressive (AR) models of different orders. Elongation direction labels from the HMM-segmented trajectories were used to rotate all segments into the same coordinate axis (as defined by the elongation direction). Each AR model was fit using all but one segment and then residual error was assessed on the withheld segment. This was repeated over all segments and the mean residual calculated for each order n . The minimum of the curve (at $n = 6$) indicates the AR model order that best predicts subsequent velocities in a novel trajectory.
- B:** Coefficients for the AR(6) model. These coefficients α_i predict the next velocity as a function of recent velocities: $\vec{v}_t = \sum_i^n \alpha_i \vec{v}_{t-i}$.

Figure 1

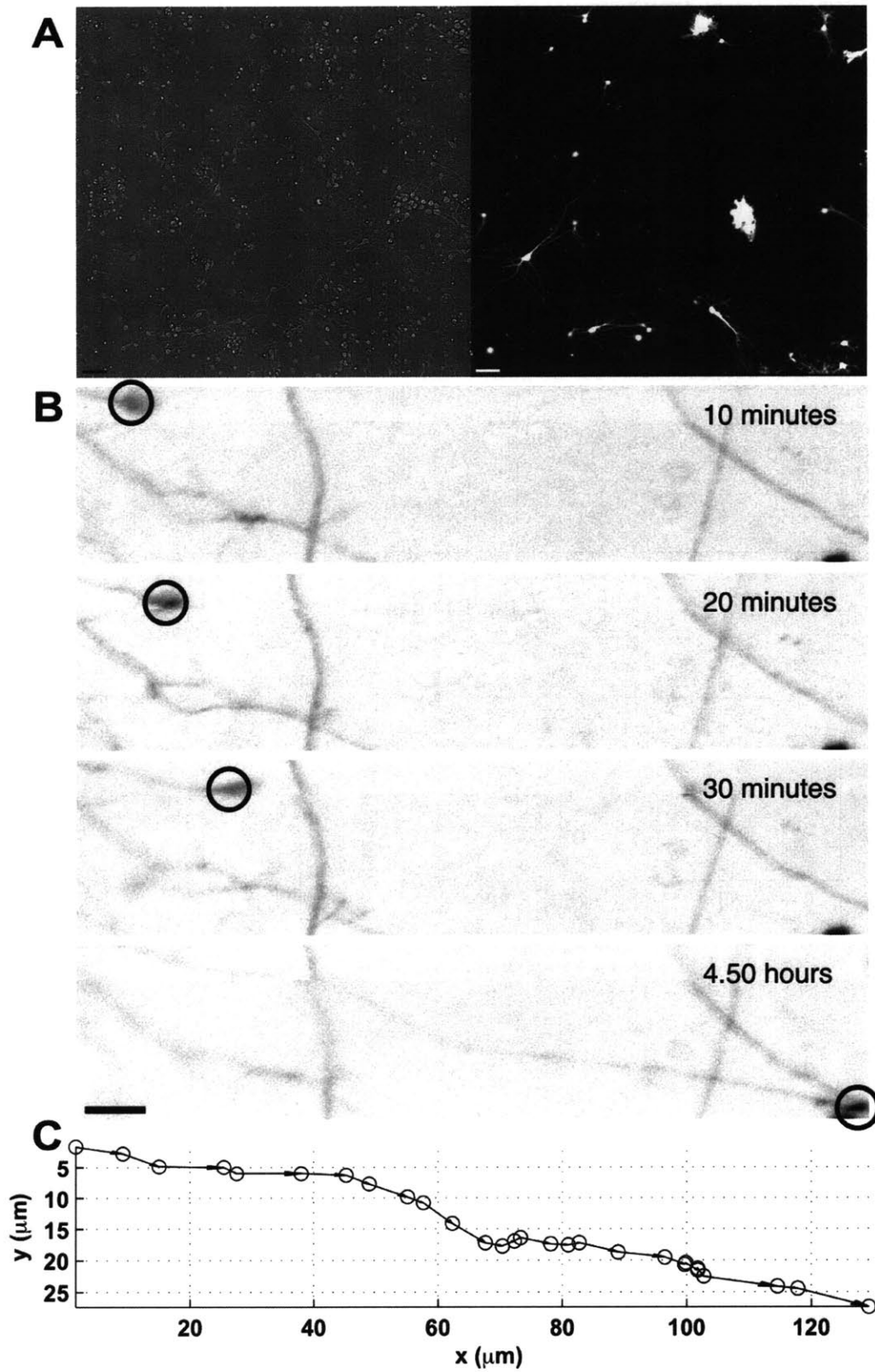
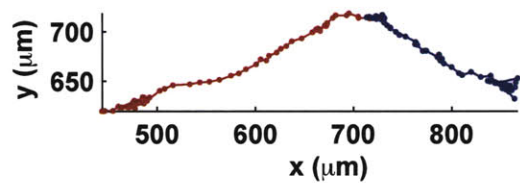
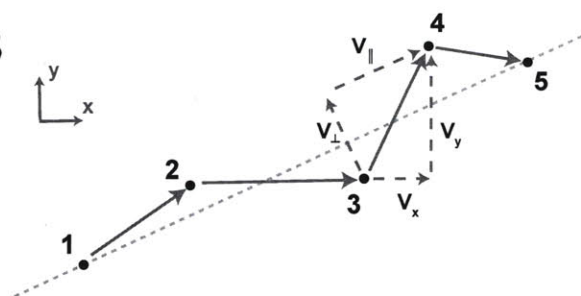


Figure 2

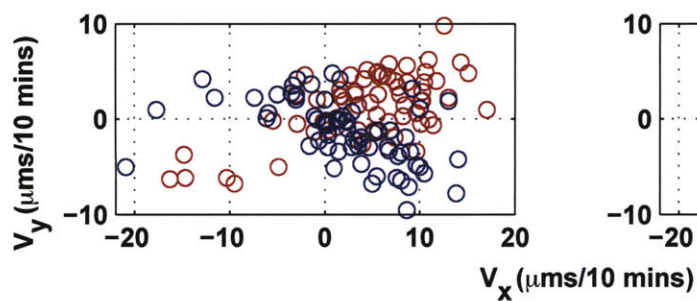
A



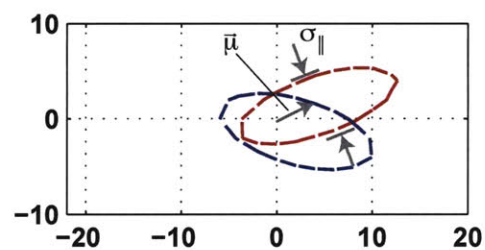
B



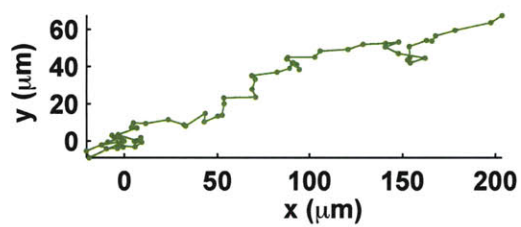
C



D



E



F

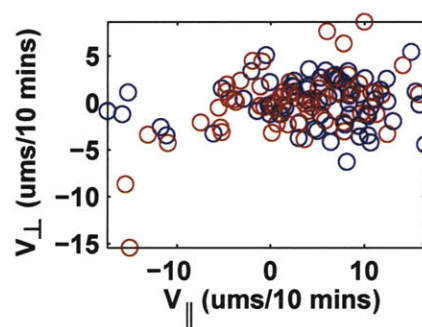


Figure 3

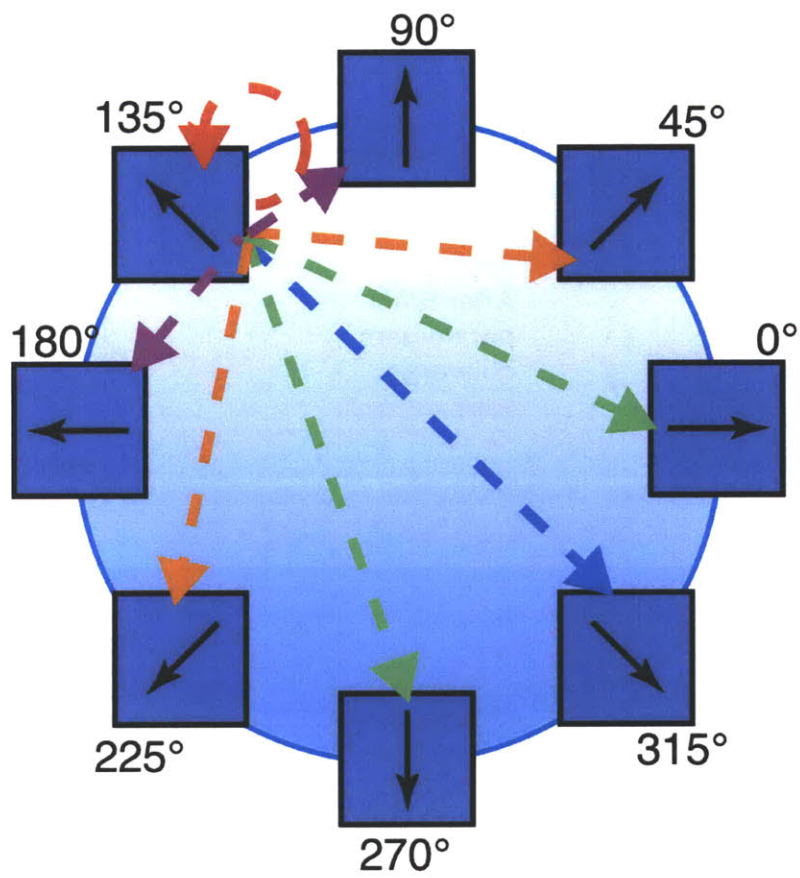


Figure 4

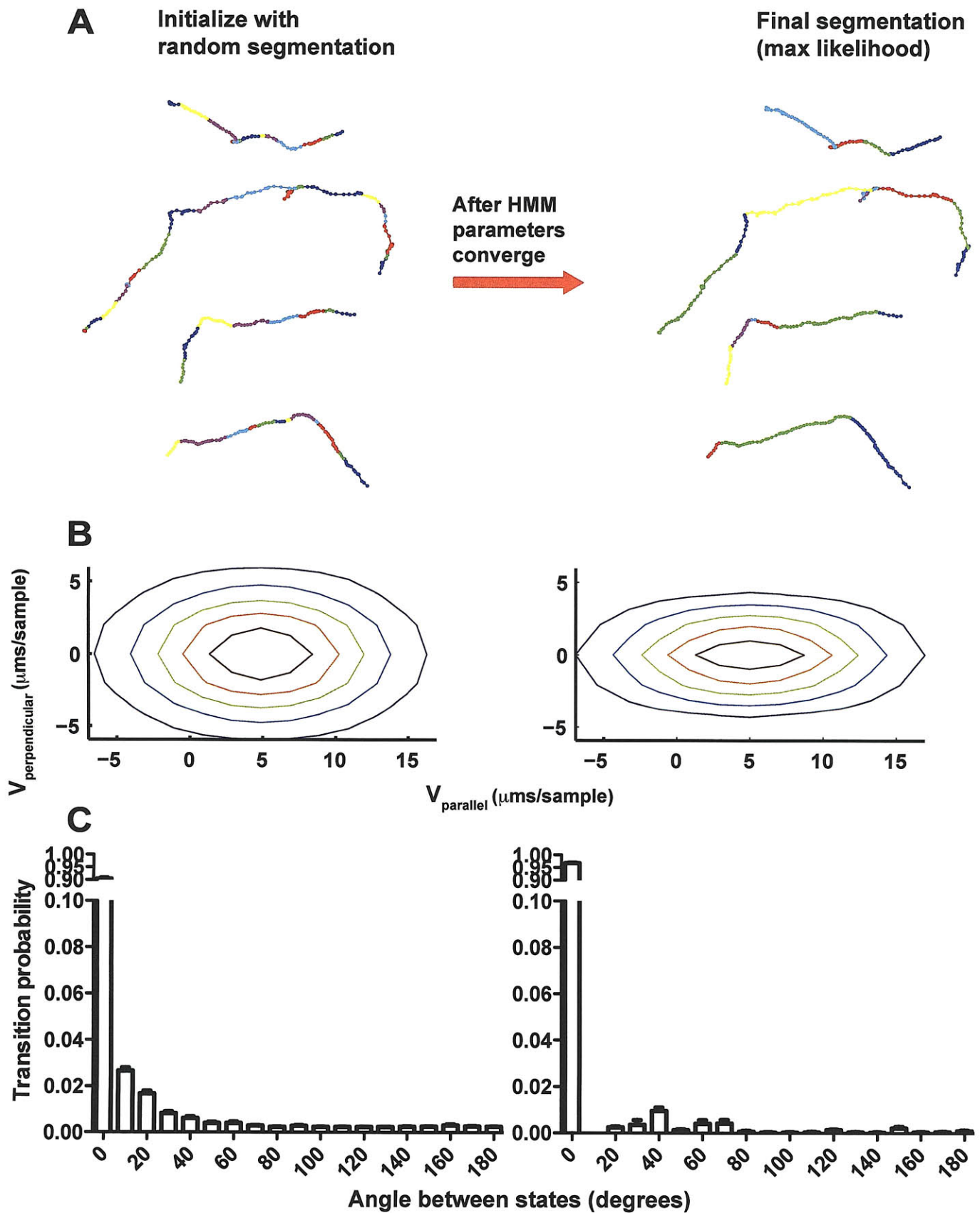


Figure 5

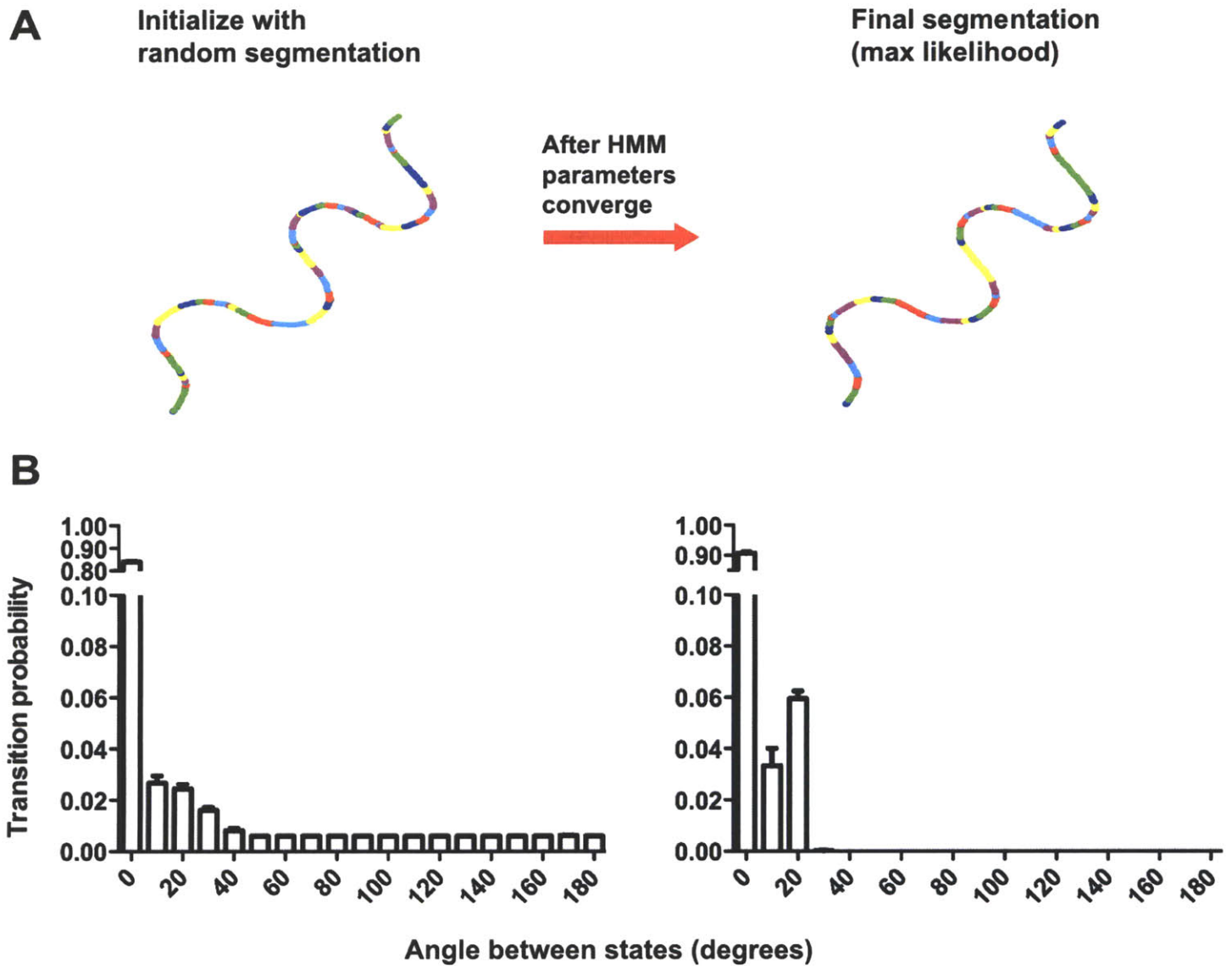


Figure 6

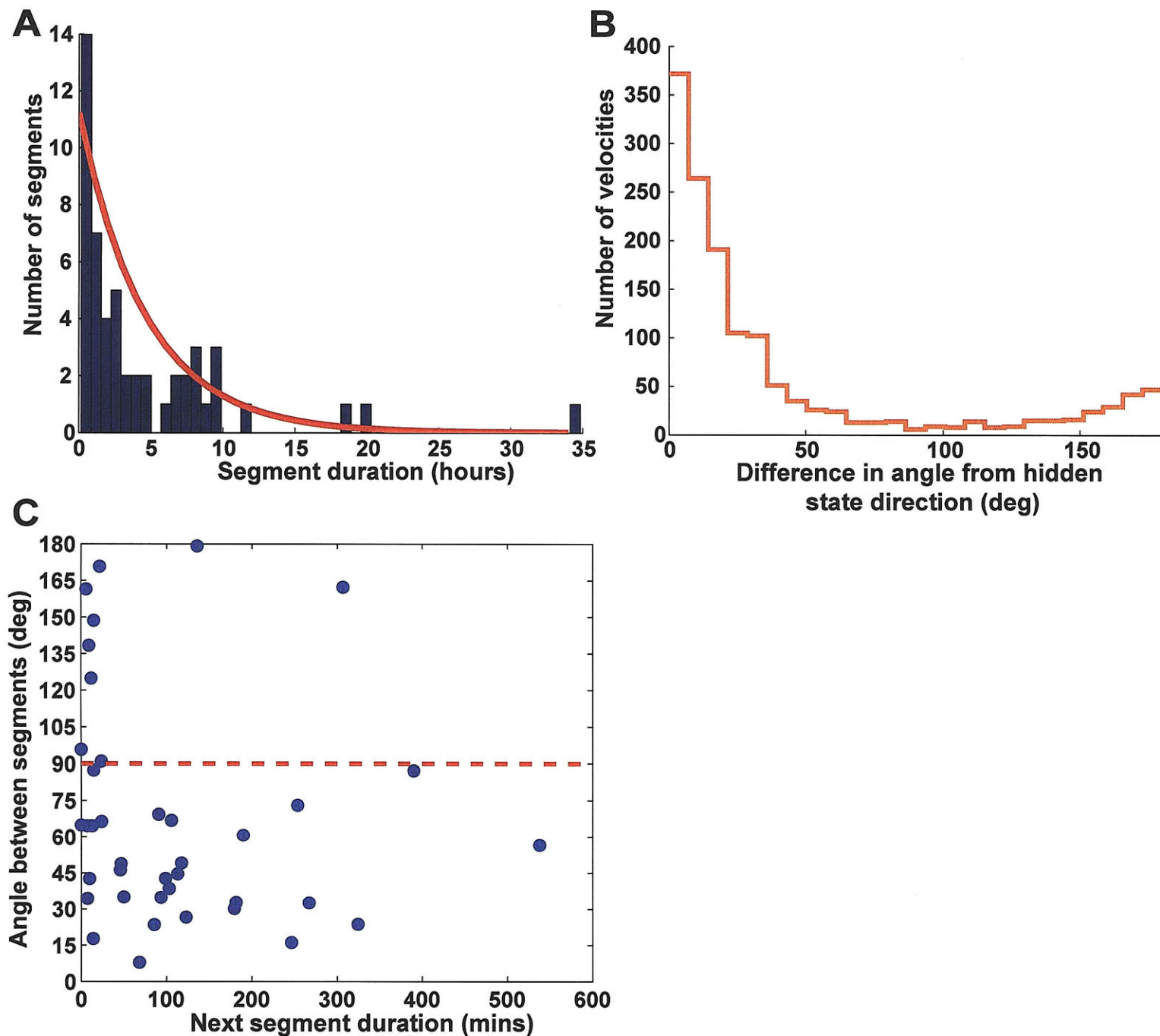
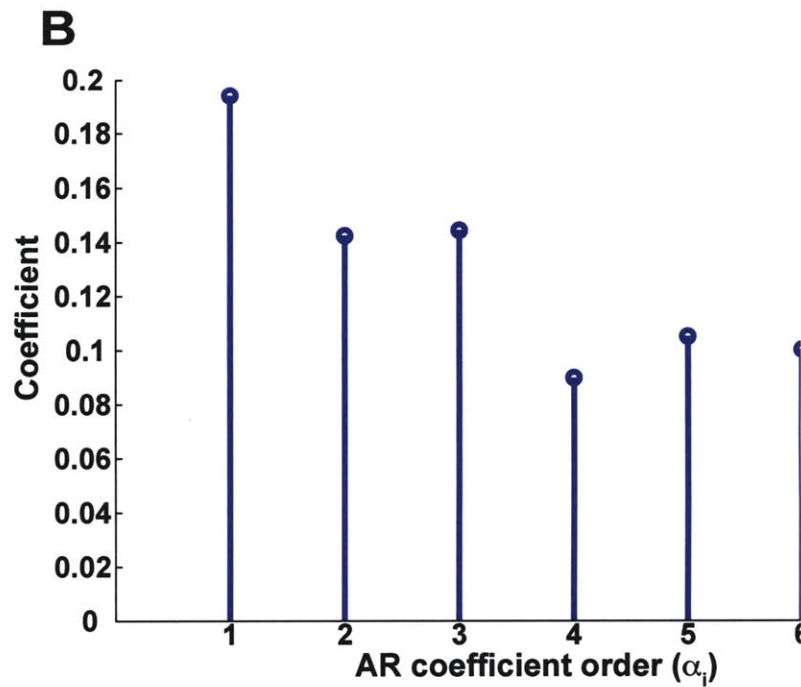
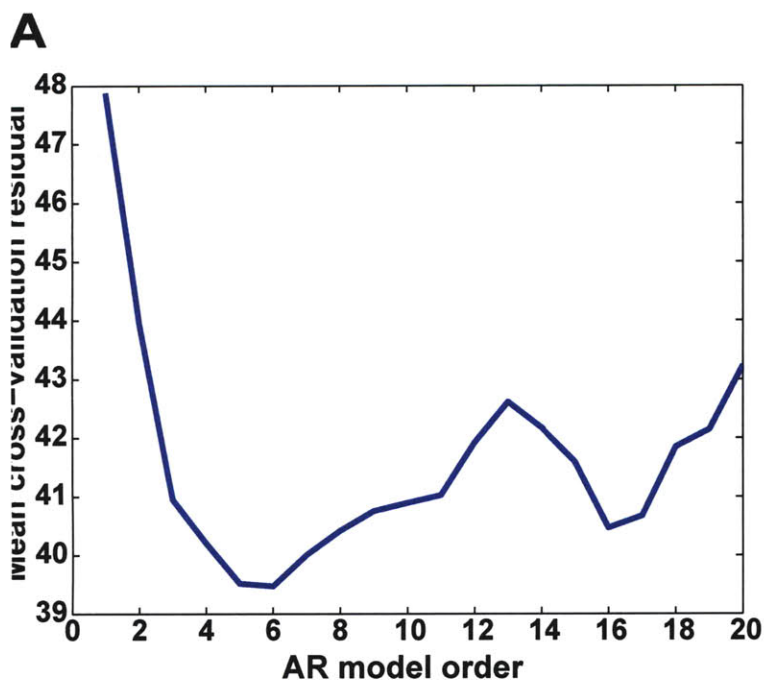


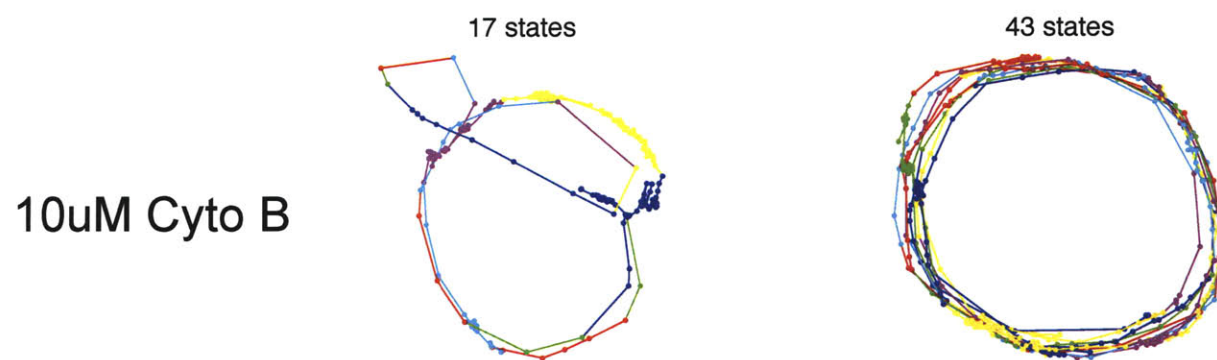
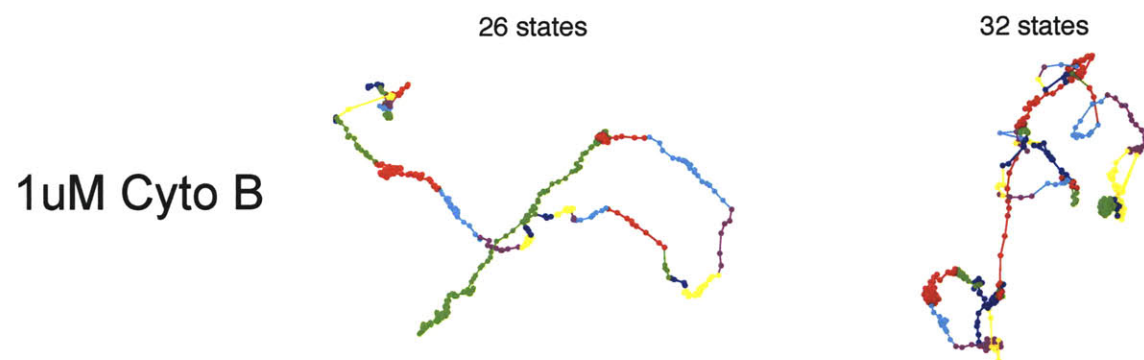
Figure 7



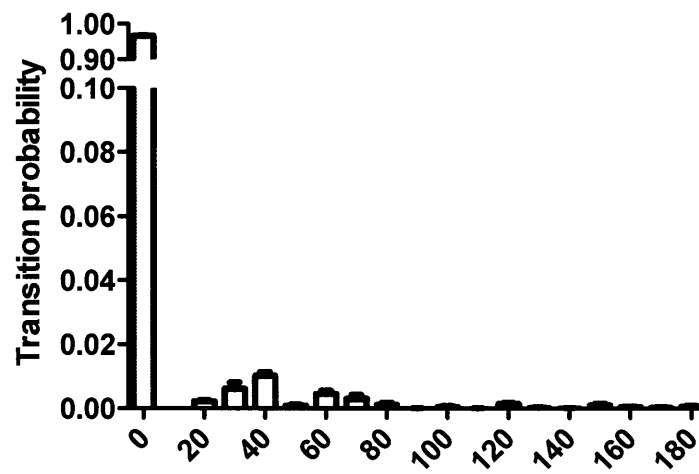
Chapter 4

Using stochastic modeling to detect changes in elongation behavior

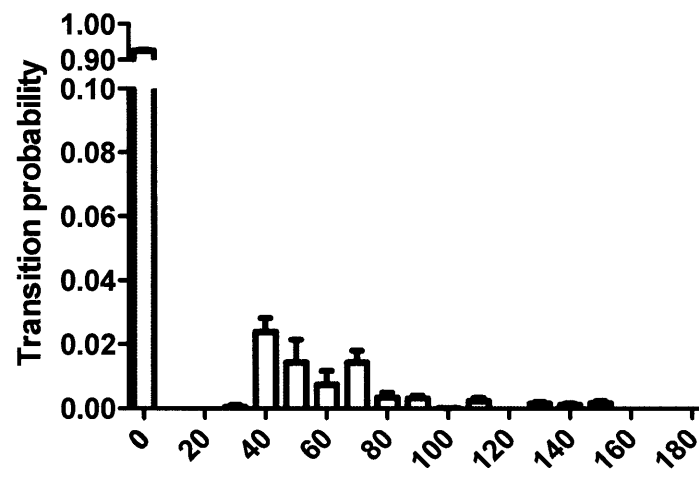
Actin manipulations: Representative segmentations



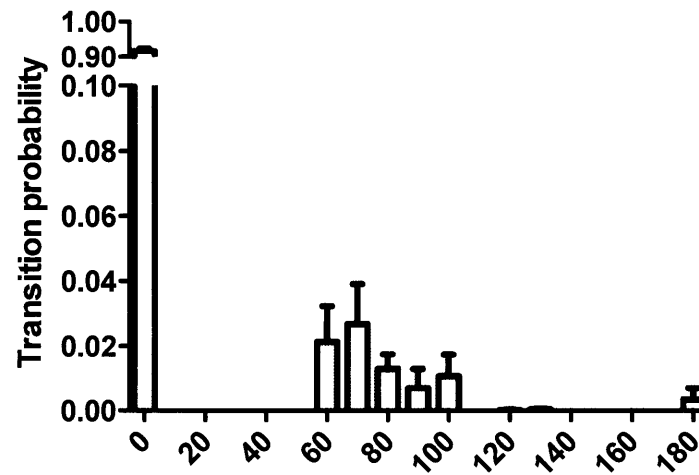
Control (no cytoB)



1uM cytoB

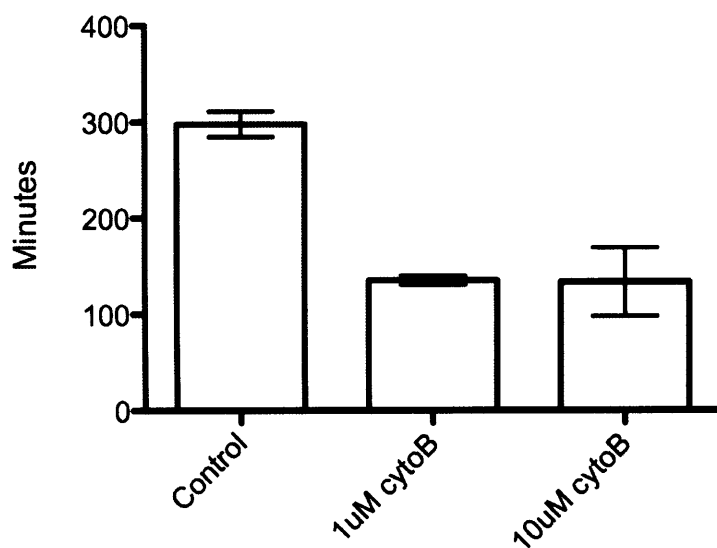


10uM cytoB

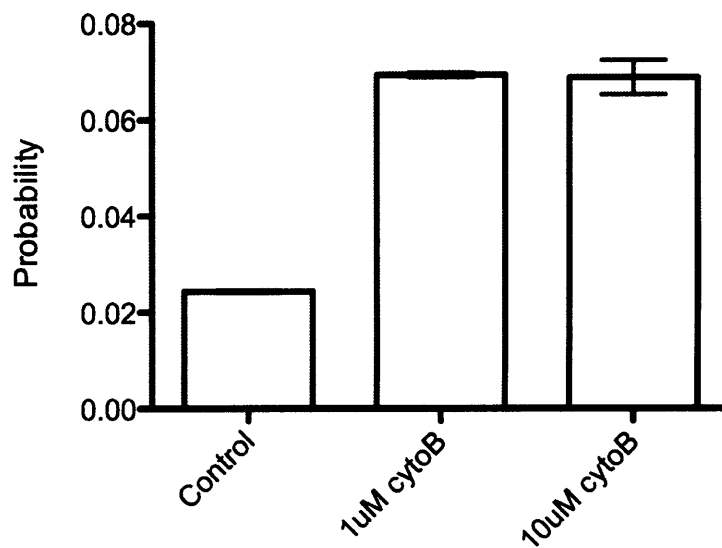


Angle between states (deg)

Mean single bias duration

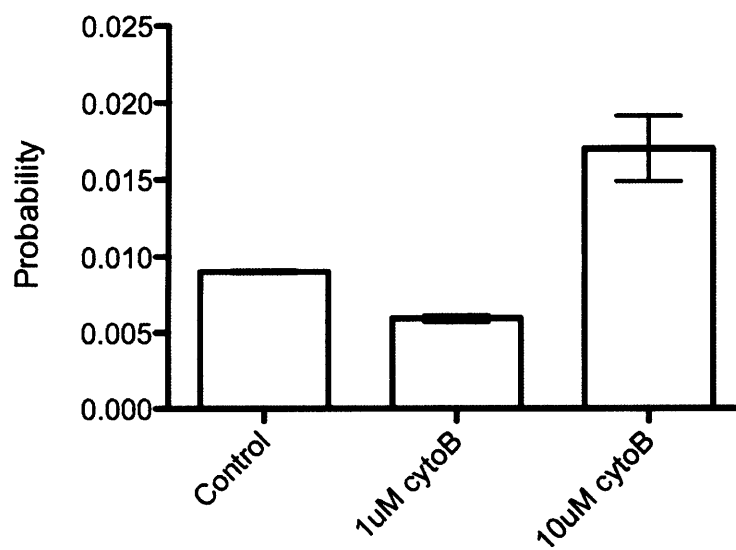


Turn probability ($\Theta \leq 90^\circ$)

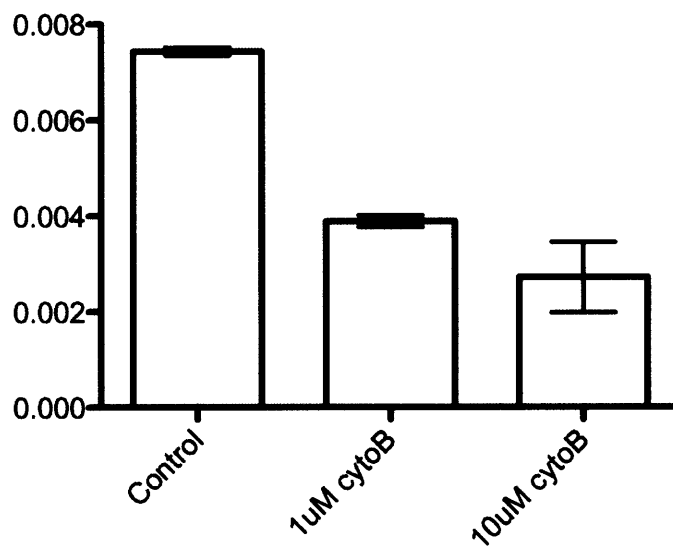


Retraction probability

$\Theta > 90^\circ$



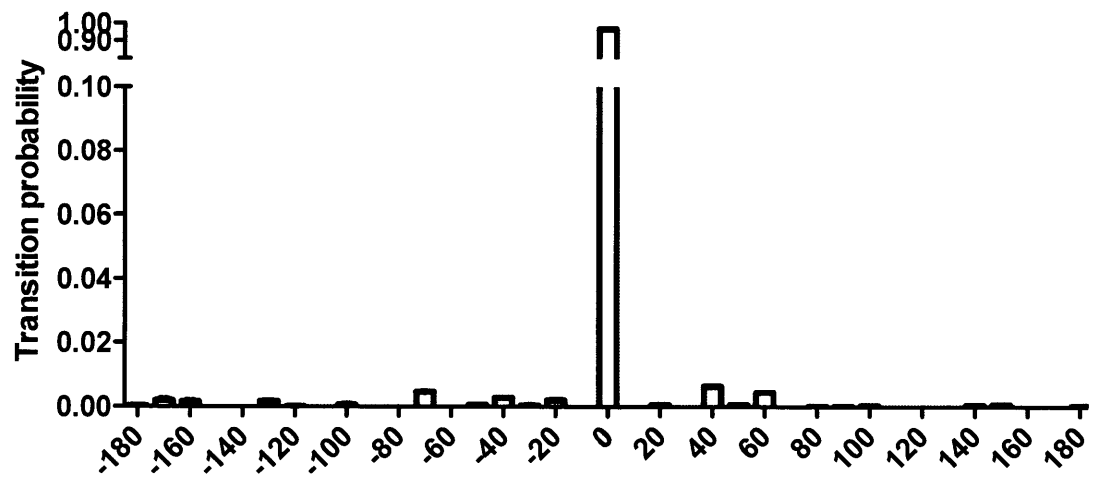
$\Theta > 120^\circ$



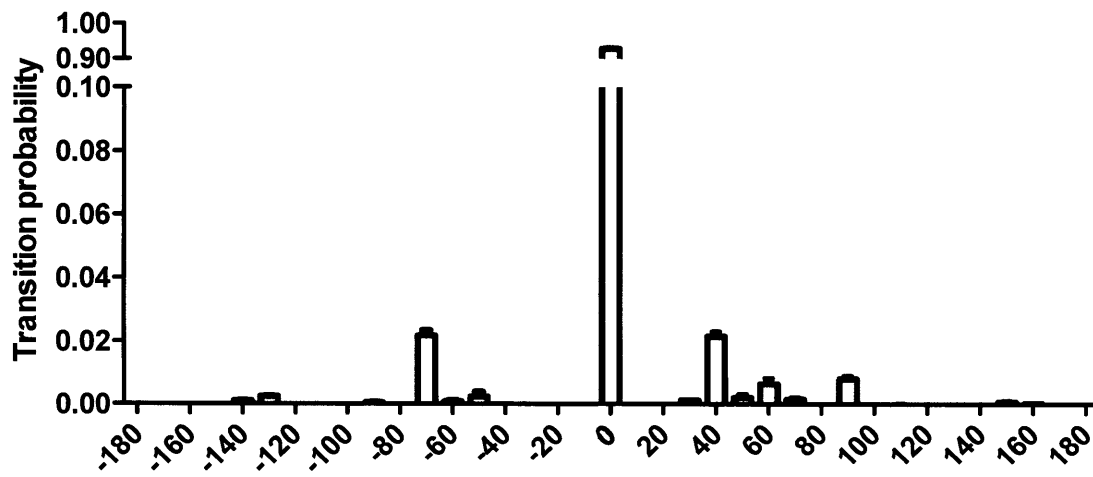
Treatment

Error bars are 95% confidence intervals of the mean distributions.

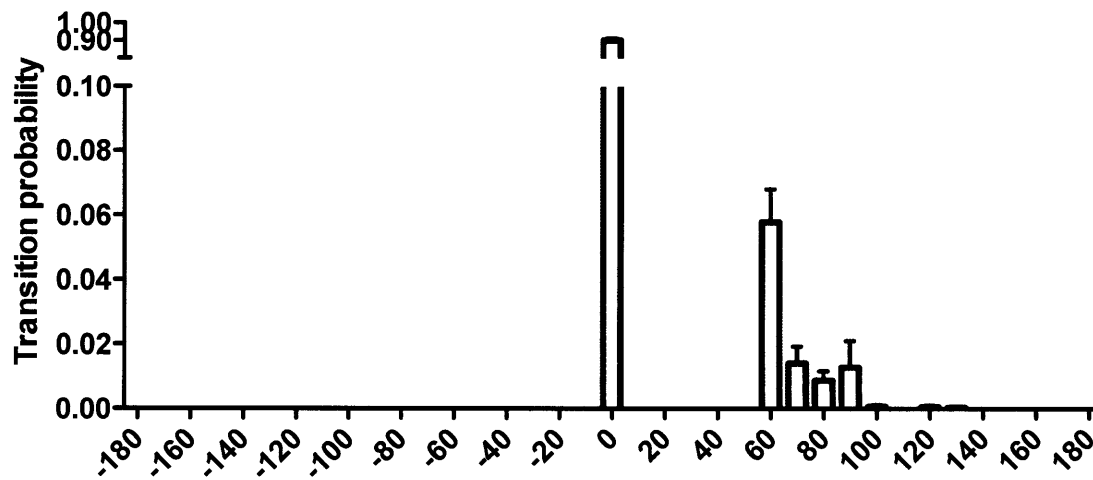
Control (no cytoB)

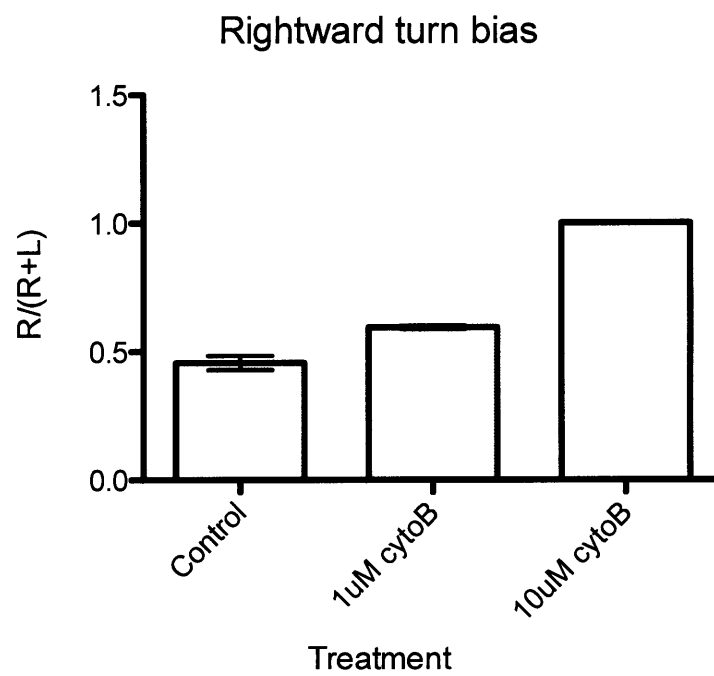


1uM cytoB



10uM cytoB





Chapter 5

Conclusion

We were motivated to find a better description of growth cone behavior to help understand mechanisms of outgrowth and pathfinding. Our unorthodox application of stochastic modeling to extended time-lapse observations of mouse cortical axon growth cones shows that the growth cones elongate along remarkably straight paths for multiple hours punctuated by sharp turns of about 40° . Surprisingly, in a culture environment where long-range cues (eg. layer- and region-specific) are absent, growth cones continue to elongate in the same direction on average for about 4 hours (extending $>100\mu\text{m}$).

5.1 Interpretations of the hidden state

Despite the variability in growth cone movement within a single segment, the growth cone keeps to a straight trajectory. The hidden Markov model captures this directional persistence with its memory of the current direction as the hidden state. Although we have presented the growth cone behavior as an observation without reference to mechanism, it is tantalizing to think about potential sources of the hidden state. Broadly, there are two possibilities: an intrinsic memory or default growth program in the growth cone that keeps it moving straight; or a directed, external signal that the growth cone can faithfully track. Both possibilities are fascinating.

Growth cones are already known to have some complex behaviors but internal memory for remembering a heading independent of the extracellular environment has not been shown. However, intrinsic growth behaviors have previously been observed both *in vitro* and *in vivo*. Cultured retinal ganglion cells grow dendrites that cover space uniformly - as they do *in vivo* - through a nontrivial growth strategy, resulting in a final dendrite geometry that is different from cortical neurons cultured in the same environment (Montague and Friedlander, 1989). A quantitative *in vivo*, two-photon time-lapse analysis concluded that mouse thalamocortical and Cajal-Retzius axons have different intrinsic growth programs because the axons have different behaviors (growth cone structure, axon trajectory and growth rates) when elongating through the same layer 1 territory (Portera-Cailliau et al., 2005). These observations lend further support to the possibility of a default growth program favoring straightness or a persistent "growth cone memory" for direction.

Of course, from our observations, it is just as likely that the directional persistence

may come from the environment. There are many examples of guidance by target-derived chemotropic cues *in vivo*, such as retinotopic mapping in the tectum and midline decussation in the spinal cord, but the *in vitro* culture environment disrupts the orderly arrangement of cell types. If reliable target-derived cues are present even after tissue dissociation, then growth cones must have sophisticated chemoreception machinery to allow them to elongate toward the correct targets without being derailed by cues from other nearby cells. Our naive expectation in the disordered environment of cell culture would be negligible directional persistence and instead constant turning. Since that is not what we observe, further experiments need to be performed to find a mechanism for straight elongation in an environment without clear guidance cues.

5.2 What is the cause of straightness?

Although there is persistence in a single direction, it is important to note that within these straight segments the heading of the growth cone can be quite variable at each time point. Figure 6B shows the distribution of angles relative to their hidden state direction (0° means the actual velocity is perfectly aligned with its hidden state direction). Individual movements can differ greatly from the hidden state direction: The median deviation is 17° and 24% of movements within segments deviate by greater than 45° .

5.3 Straightness as a metabehavior of elongation

The straightness of the growth cone paths is impressive for another reason. Since our labeling technique is unbiased, the straightness behavior is shared by many (possibly all) types of cortical axons. Most labeling techniques - even labels that seem to be distributed randomly such as the Thy1 fluorescent protein mouse lines (Feng et al., 2000) - target genetically defined (though potentially unknown) subclasses of neurons. Popular viral techniques, such as herpes simplex or pseudorabies virus, have different tropisms, preferring to label certain neurons over others (Barnett et al., 1993; Card et al., 1997). Existing unbiased labeling techniques in culture, such as calcium phosphate transfection, lipofection, electroporation and biolistics, are more toxic, often causing axon retraction and cell death (Craig, 1998; McAllister, 2000). By mechanically mixing neurons from a completely labeled cortex with neurons from a completely unlabeled cortex, our labeling is less biased than previous techniques without such toxicity.

One might expect that particular outgrowth and guidance behaviors would only be found in certain genetically similar subpopulations of axons, but our analysis suggests that the preference for straight trajectories is a metabehavior, common to all cortical axons. This metabehavior has been observed before. Katz was the first to explicitly document the straightness of axonal growth cones in cultured frog and chick peripheral neurons (1985). In the neocortex, others have shown that axons of pyramidal neurons, but not interneurons, follow straight trajectories (Thomson and Morris, 2002; Portera-Cailliau et al., 2005).

5.4 In vivo vs. in vitro

One criticism is that we have observed these behaviors in vitro. The observations were made in vitro out of necessity, as it would be difficult, if not infeasible, to image and track individual neocortical axons in vivo with the same temporal frequency for days over a millimeter-scale region for multiple reasons (eg. anesthesia duration, field of view, finding the same growth cones over repeated sessions, etc.). Nevertheless, it is imperative to know if the observed behaviors are also seen in the developing cortex in vivo. We cannot be sure, but previous in vitro axon outgrowth behaviors have been confirmed in vivo. For example, the individual stages of axon elongation via lamellapodial advance, originally described in cultured *Aplysia* neurons (Goldberg and Burmeister, 1986), were verified in the T11 pioneer neurons of the embryonic grasshopper limb (Sabry et al., 1991) and indeed seem to be general to many types of axons (Dent and Gertler, 2003).

5.5 Stochastic models for quantifying cellular behavior

Although we use the HMM as a tool for testing hypotheses about growth cone turning behavior, it is sensible to ask in which ways the learned model is really a quantitative and accurate model of axon elongation. For quantification purposes, the HMM approach provides a new assay for neurite behavior. Within individual segments, the parameters of the emission distribution quantify the mean rate of elongation and the expected deviations in the directions parallel and perpendicular to the elongation direction. These deviations can be interpreted as a measure on how willing the growth cone is to explore its environment. The transition probabilities measure how often the "true" heading of the growth cone changes and what turning angles are most likely during those changes.

But does the HMM provide an accurate model of axon elongation? In some ways, it does. For example, generated trajectories from the learned model look similar to real axons (see Supplementary Figure 4), though real axons seem to have a greater propensity for self-avoiding paths. This is to be expected since long-term dependencies are not captured by the HMM. Also, as can be inferred from the learned transition probabilities (Figure 4C) and seen in some of the segmented growth cone paths (Figure 4A), occasionally retractions are segmented into separate hidden directions instead of being captured purely in the emission probabilities for the elongation direction.

Chapter 6

Appendix: A fast flexible ink-jet printing method for patterning dissociated neurons in culture

This chapter was previously published as: Sanjana, N.E. and Fuller, S.B. (2004). A fast flexible ink-jet printing method for patterning dissociated neurons in culture. *Journal of Neuroscience Methods* 136:151–163.

A fast flexible ink-jet printing method for patterning dissociated neurons in culture

Neville E. Sanjana^{a,1}, Sawyer B. Fuller^{b,*,1}

^a Department of Brain and Cognitive Sciences, Massachusetts Institute of Technology (MIT), Cambridge, MA, USA

^b Department of Mechanical Engineering and Center for Biomedical Engineering, E25-425, MIT, 77 Massachusetts Avenue, Cambridge, MA 02139, USA

Received 17 October 2003; received in revised form 9 January 2004; accepted 9 January 2004

Abstract

We present a new technique that uses a custom-built ink-jet printer to fabricate precise micropatterns of cell adhesion materials for neural cell culture. Other work in neural cell patterning has employed photolithography or “soft lithographic” techniques such as micro-stamping, but such approaches are limited by their use of an un-alterable master pattern such as a mask or stamp master and can be resource-intensive. In contrast, ink-jet printing, used in low-cost desktop printers, patterns material by depositing microscopic droplets under robotic control in a programmable and inexpensive manner. We report the use of ink-jet printing to fabricate neuron-adhesive patterns such as islands and other shapes using poly(ethylene) glycol as the cell-repulsive material and a collagen/poly-D-lysine (PDL) mixture as the cell-adhesive material. We show that dissociated rat hippocampal neurons and glia grown at low densities on such patterns retain strong pattern adherence for over 25 days. The patterned neurons are comparable to control, un-patterned cells in electrophysiological properties and in immunocytochemical measurements of synaptic density and inhibitory cell distributions. We suggest that an inexpensive desktop printer may be an accessible tool for making micro-island cultures and other basic patterns. We also suggest that ink-jet printing may be extended to a range of developmental neuroscience studies, given its ability to more easily layer materials, build substrate-bound gradients, construct out-of-plane structure, and deposit sources of diffusible factors.

© 2004 Elsevier B.V. All rights reserved.

Keywords: Patterned neural networks; Ink-jet printing; Surface chemistry; Cell attachment; Cell growth control; Dissociated cell culture; Glia patterning; Hippocampus

1. Introduction

Our understanding of the cellular basis of learning and memory has been aided by the use of in vitro neural cell culture—the growth of neurons in a controlled environment outside of the living organism. Dissociated cell culture contrasts with explant culture, brain-slice, and in vivo preparations in that the physical structure of the tissue is lost during enzymatic and mechanical digestion. Once the dissociated neurons settle they may adhere to the culture surface (the “substrate”), where they re-grow processes and form synapses with other neurons. The growth of these

processes, the migration of cell bodies, and other in vitro phenomena may be influenced by fabricating patterns of chemicals and/or physical structure bound to the substrate. Patterned cell culture may be used for studying smaller isolated networks, developmental cues, or single-cell properties. A long-term goal is to utilize substrate-bound patterns of biomaterials as a simulation environment and test-bed for analyzing biological signals encountered by neurons undergoing development.

Early work in patterned neuron cultures employed small islands of adhesive protein or cells arranged over an inhibitory background such as agarose gel so that each island contained a small number of neurons. Such cultures simplified studies of synapses between neurons and cardiac myocytes by limiting connections in several of the myocytes islands to a single neuron (Furshpan et al., 1976). Though the technique relied on a relatively simple airbrush

* Corresponding author. Tel.: +1-617-452-2691; fax: +1-617-452-2913.

E-mail address: minster@mit.edu (S.B. Fuller).

¹ Both authors contributed equally to this work.

procedure to generate the tiny droplets, the sizes and locations of the islands were arbitrary, and only round islands could be produced. Newer, more controlled patterning techniques have included contact masks (Westermarck, 1978), photolithography using photoresists (Kleinfeld et al., 1988; Wyart et al., 2002) and photochemistry (Hickman et al., 1994), microstamping (Branch et al., 2000; Scholl et al., 2000; Wheeler et al., 1999), and microfluidic channels (Martinoia et al., 1999). However, these techniques share a limiting characteristic in that they rely on the existence of an un-alterable master pattern and so limit experimentation with different patterns. To change the pattern master to fit changing experimental needs may require multiple days or even weeks, which can be especially problematic when iterative refinement is necessary or when under an experimental deadline.

To overcome this and other limitations, we introduce ink-jet printing as a method for fabricating patterns of materials to influence neuron growth. In contrast to desktop ink-jet printers which print dyes or pigments onto paper, we print biologically-active materials onto coverslips. Ink-jet printing has the advantage that the pattern is stored entirely in digital form and can be altered and re-printed in minutes. This flexibility is absent from the master pattern-based approaches. In addition, and perhaps more importantly, because it is fundamentally different than the above techniques, it has unique advantages for neuroscience research: Compared to master pattern-based approaches, ink-jet printing makes it much easier to deposit multiple layers of different materials, build out-of-plane structure, deposit large amounts of material, and fabricate substrate-bound gradients, as well as being relatively inexpensive.

Though the resolution of ink-jet printing is low (tens of microns) relative to the lithographic techniques described above (sub-micron), we feel there is a need for patterning in a co-culture environment with glia. In addition, co-culture of neurons with glia provides a more biologically plausible environment *in vitro*. Glia are more difficult to confine to patterns with micron-sized features (St John et al., 1997; Wyart et al., 2002), and thus the resolution of the printer we present is closer to the resolution limit for glia co-culture. In addition, we will show that it is possible to create features significantly smaller than the size of a single droplet by printing negative relief, in which spaces between droplets become the features instead of the droplets themselves.

In this work, we demonstrate one of the first uses of ink-jet printing for influencing the behavior of neural cells in culture by using it to print improved micro-island culture patterns (Roth et al., *in press*; Turcu et al., 2003). We describe a flexible surface chemistry procedure and a dissociated hippocampal cell culture protocol suitable for patterning cell adhesion biomolecules on a cell-repulsive background. We present results for these protocols that demonstrate the patterned growth of healthy neurons for periods as long as 3 weeks. We quantitatively assess neuron compliance with printed patterns from 5 to 25 days in culture. In addition,

using intracellular recording and immunocytochemistry we show that patterned cultures are similar to un-patterned cultures in passive membrane properties, resting potentials, synaptic density, and inhibitory cell density. Lastly, we suggest that such patterns may be fabricated using a much less complex desktop printer, and that custom hardware such as is reported here could be used for neural development studies.

2. Methods

2.1. Ink-jet printer design

Ink-jet printing consists of depositing single, tightly-controlled microscopic droplets 10–100 μm in diameter onto a substrate. While continuous-jet printers expel a continuous pressurized stream that breaks up into small droplets, drop-on-demand (DOD) printers, such as the one reported here, eject single droplets in response to a pressure impulse in the ink chamber (Heinzl and Herz, 1985). The pressure impulse is generated by a piezo crystal that deforms in response to a voltage pulse generated under computer control. The droplet takes a 1–10 mm ballistic trajectory to the substrate, where it lands and adheres. The liquid evaporates, leaving a round deposit of solid material. The print head is moved robotically over the substrate as droplets are ejected, leaving a pattern of round dots (Fig. 1).

Ink-jet printing has recently been employed in a range of fabrication applications, such as three-dimensional object fabrication (Z Corporation, Cambridge, MA; 3D Systems, Valencia, CA), printed electronics and micro-mechanical structures out of nanoparticle-based inks (Fuller and Jacobson, 2000; Fuller et al., 2002), and organic light-emitting diode (OLED) displays (Cambridge Display Technology, Cambridge, UK). In the biosciences, ink-jet printing has been used to print patterns of fibronectin for cell micropositioning (Klebe, 1988), growth factors for myoblast cells (Watanabe et al., 2003), three-dimensional cell scaffolding for liver cells (Griffith et al., 1997), cast collagen gels into ink-jet printed wax molds for cell culture (Sachlos et al., 2003), and whole mammalian cells (Wilson and Boland, 2003). Here, we apply the technology to arranging chemical patterns for controlling and assessing the properties of neurons in culture.

For this particular purpose, we developed both a custom-designed printer and MS Windows-based computer aided design (CAD) software environment (Figs. 2 and 3). The printer was designed to enable a wider range of studies than would be possible with off-the-shelf desktop printer hardware. For instance, a custom printer nozzle with a single orifice was used so that print head priming volumes were smaller than 1 ml, allowing us to print biomaterials for which only small quantities were available. Drawings were specified in a vector-based format consisting of points and lines of droplets, which was a simple yet sufficiently capable system for the work described here. In addition to requiring

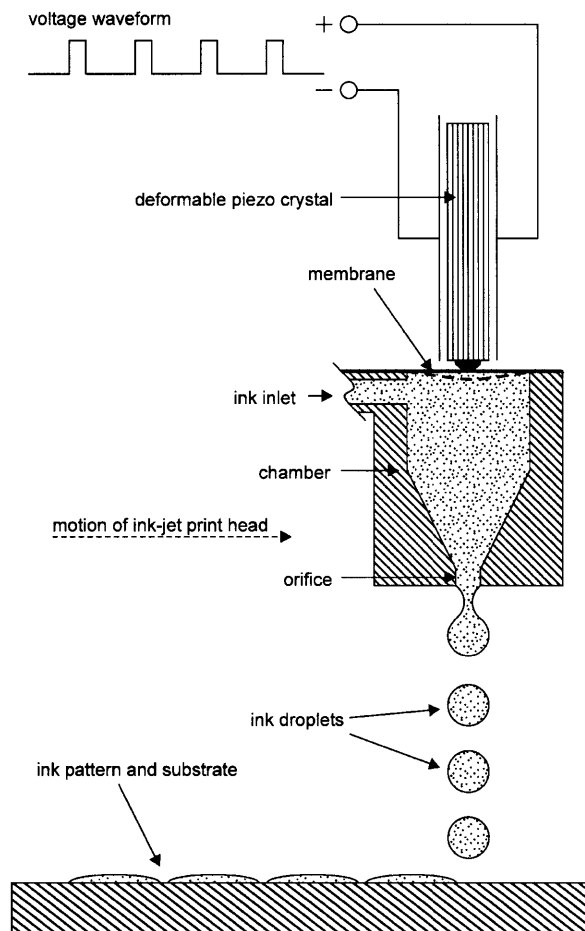


Fig. 1. Diagram of the operation of a piezo drop-on-demand ink-jet print head. Microscopic ink droplets are ejected individually through an orifice by means of a pressure impulse delivered by a piezo crystal. Each droplet, 10–100 μm in diameter, takes a ballistic trajectory a small distance ($\sim 1\text{ mm}$) to the glass substrate. The print head is moved robotically in two-dimensions above the substrate as droplets are ejected, leaving a pattern of round dots on the substrate.

less liquid for priming, using a single nozzle required less software and hardware, was less prone to failure when attempting to use new, experimental “inks,” and could position individual droplets with more precision than a rasterizing printer. The entire printer was made as small as possible and was controlled by a laptop computer so it could be moved easily, such as into a sterile laminar flow hood or a cold room.

The nozzle was procured from Microfab Technologies, a manufacturer specializing in ink-jet printing research (Fig. 3, inset). The nozzle used an annular piezo crystal that “squeezed” a glass tube to eject droplets. The tip was drawn to an orifice diameter of 30 μm (model MJ-AB-030). Inks could be water- or solvent-based with a solids density less than or equal to 2.5 mg/ml. The ink feed for the print head consisted of a 20 cm length of small-diameter Tygon tubing connecting the barbed fitting of the print nozzle to a dulled syringe needle with a luer fitting to a 5 ml syringe. Manual manipulations of syringe pressure were used to generate pressure differentials at the print-head. Voltage pulses to the

head to eject droplets were generated by custom-designed high-voltage hardware with a proprietary serial RS-232 command set (Microfab Technologies, model JetDrive III). The voltage impulse to eject a droplet of water-based “ink” was 28 V for 20 μs . Droplet ejection frequencies ranged from 1 to 500 Hz.

The print head was fixed over a moving substrate support riding on roller bearings and actuated by two perpendicular leadscrew-driven servomotors (Newport Corp. model 850-G-HS) driving the X- and Y-axes. A three-axis closed-loop stage controller (Newport Corp. model ESP-300) coordinated the motion of the two motors. Motion commands and jet pulse commands were sequentially generated and orchestrated by the custom-written CAD software environment based on drawing data. The printing surface was horizontal, allowing the substrate, such as a round glass coverslip, to be positioned on top. The temperature of the substrate was optionally controlled using a closed-loop controller (Watlow, series 965) and a temperature-detecting thermocouple. The controller used a power relay in pulse-width modulated mode driving a peltier device (TE Technology) in either positive bias (cooling) or negative bias (heating). The peltier device was bonded with a thermal adhesive to a PC microprocessor heatsink of sufficient thermal capacity.

2.2. Ink-jet printing procedure

Prior to printing, all surfaces in contact with the substrate were sterilized with a 70% ethanol solution, including the printing surface upon which the substrate was placed, the ink feed, and the nozzle orifice itself. The nozzle was back-flushed for 30 s with 70% ethanol in water to sterilize and then back-flushed for 30 s with Millipore water. Back-flushing and ink loading were achieved by generating negative pressure in the syringe to pull liquid in through the small tip of the nozzle, effectively filtering it to the nozzle size. The nozzle was then loaded with 200–500 μl of ink. Once loaded, the ink was forcibly ejected from the orifice for a short time to insure that no bubbles remained and that the orifice was clear of debris. Pressure in the ink feed was then equalized to atmospheric pressure by opening a valve connected to the syringe. A lint-free cloth was used to remove excess liquid from the tip of the head and then the head driver box was commanded to send pulses at 1 kHz, generating a barely-visible stream of droplets that could be judged for quality. If droplets were ejecting diagonally, or not at all, more ink was forcibly ejected to clear any nozzle debris and the pressure was again equalized. Once the stream was satisfactory, the print head driver hardware was set to eject droplets at 10 Hz continuously to insure that the nozzle did not dry out and clog during periods of inactivity.

Drawing files usually included a ring of large islands printed around the periphery. The islands were visible to the naked eye, providing visual feedback during printing that the nozzle was still ejecting droplets and had not dried out or clogged. In addition, islands on the perimeter served to

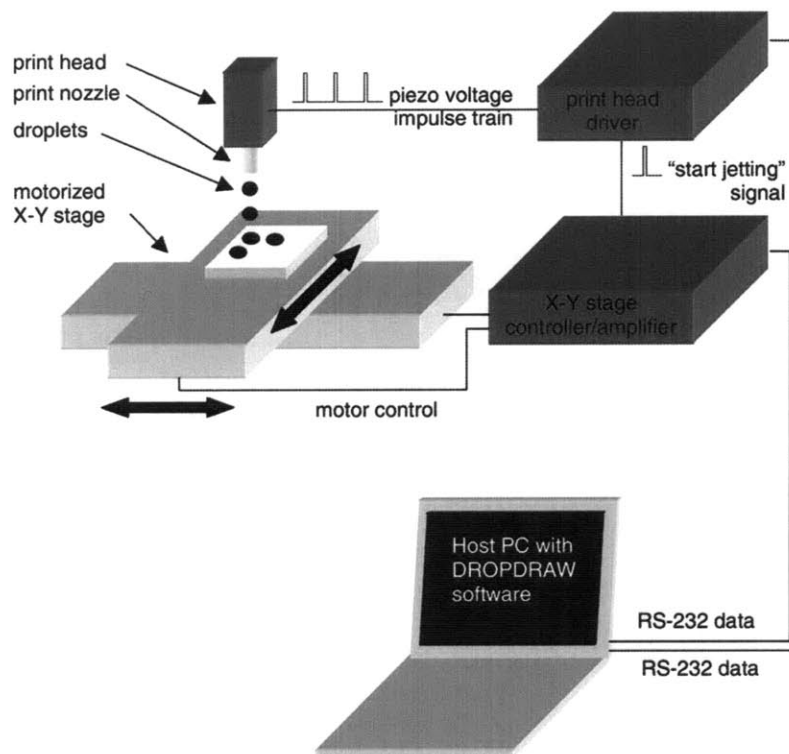


Fig. 2. Schematic of the elements of the custom-built ink-jet printer used in this work. A PC with a custom-written software environment sends data through a serial port to command an X-Y stage servomotor controller to move according to a drawing stored in the software. When a commanded position is reached, the stage controller sends a signal to the print head driver to generate a particular waveform specified by serial commands from the PC. This signal causes one or more droplets to be ejected from the nozzle orifice at the desired position.

spread out cultured neurons so that a disproportionate number of them were not adhering to the outer edge of the pattern of interest. After printing, the coverslips were sterilized by ultraviolet radiation for 15 min.

2.3. Pattern chemistry

A surface chemistry was needed that provided a strong contrast between cell-adhesive and cell-repulsive areas to constrain the locations of cell bodies and neurites for extended periods of time. To optimize versatility, we wanted a chemistry protocol that allowed the “ink” to be either cell-adhesive or cell-repulsive *without requiring any change in materials*. That is, either the cell-adhesive or cell-repulsive biomolecule could be used as a background coating the coverslip or as the printed foreground. For simplicity, in this work, we demonstrate only results in positive relief (cell-adhesive material patterned onto a cell-repulsive background).

The positive relief patterning process required two major components: (1) a repulsive background coating the slide entirely and uniformly that did not allow cell adhesion and (2) an adhesive molecule that remained in place on top of the repulsive background, that cells adhered to, and that could be ink-jet printed. The printed cell-adhesive material was a collagen/poly-D-lysine (PDL) mixture and the repul-

sive background was poly(ethylene) glycol (PEG) covalently bonded to the glass surface. A diagram summarizing the process is shown in Fig. 4.

The first major component, the repulsive background, had unique requirements. To achieve precise and reproducible results with ink-jet printing, the background being printed upon needed to be smooth and uniform. As mentioned, we also wanted the repulsive molecule to have the additional flexibility that it itself could be printed. For example, agarose is not easy to print by ink-jet because it dissolves in water only at high temperatures. In general, for reliable printing, the “ink” needed to be non-reactive with the print head and to be below 0.5% weight in water. For instance, other candidate inhibitory materials, such as silanes, were eliminated because they could react with the glass of the print head and change its wetting characteristics. In the future, this limitation might be circumvented with the advent of all-stainless steel, small-volume print heads.

Thus, in this work, we chose poly(ethylene) glycol as the inhibitory background material. PEG has been shown to provide long-term inhibition of cell adhesion in several previous studies of patterned neural cell culture (Branch et al., 2000; Wheeler et al., 1999). It is non-reactive with the glass print head, is non-toxic to cells when rinsed properly (see Section 2.4), and can be linked to the coverslip to form a uniform layer. The PEG background application procedure

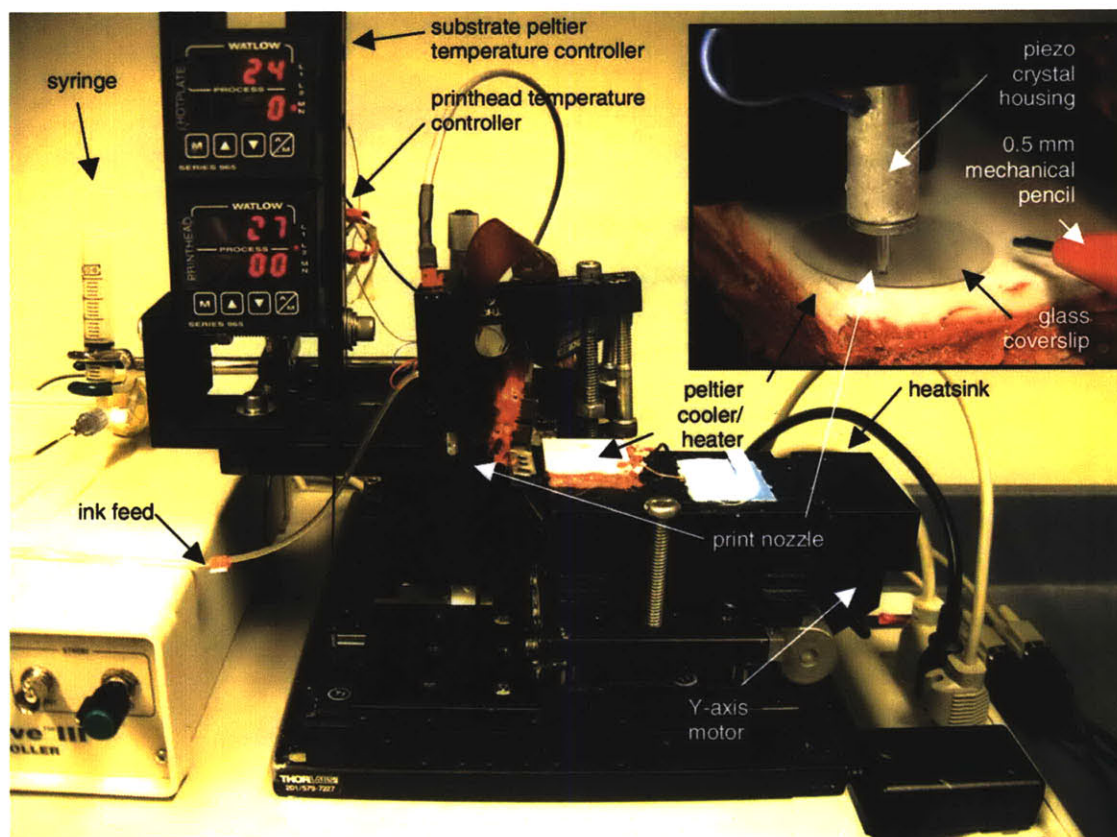


Fig. 3. Photograph of the ink-jet printer with inset detail of print nozzle. Components include X–Y servomotors, a rollerbearing stage, a peltier cooler/heater for controlling the substrate temperature, the piezo print head, ink feed, and digital closed-loop temperature controllers. The tip of a 0.5 mm mechanical pencil is included in the print nozzle detail for scale.

was adapted from a protocol in Cass and Ligler (1998) for immobilizing biomolecules containing an amino group to glass substrates.

Round coverslips (German glass, 12 mm diameter, Electron Microscopy Sciences 72196-12) were cleaned overnight in a 10% KOH solution to remove contaminants, and then soaked in a 2.5% (by volume) aqueous

solution of aminopropyltriethoxysilane (Sigma A3648) to expose reactive amino groups for 30 min and then rinsed in water and ethanol before being dried in a vacuum oven overnight at 80 °C. Coverslips were then soaked in the homobifunctional crosslinker glutaraldehyde (Sigma G7651) in a 0.1 M aqueous solution of sodium carbonate (Na_2CO_3) for 2 hours, exposing an aldehyde group that is reactive with amino groups. For the final step, coverslips were soaked in a 0.5% (by weight) aqueous solution of amino-terminated poly(ethylene) glycol (MW 5000, Shearwater Corp. 2M2V0H01) for 1–2 days prior to printing.

The second major component, the adhesive molecule, needed to fulfill three requirements. First, it needed to stay in place on top of the repulsive background. For example, we found that a synthetic extracellular matrix peptide with a RADA16-motif (arginine–alanine–aspartate–alanine) delaminated from the PEG surface despite good neuron adherence to the peptide (Holmes et al., 2000; Zhang et al., 1993, 1995, 1999). Secondly, cells needed to adhere to the molecule. Common cell adhesion substrates include collagen, poly-D-lysine, laminin, and MatriGel (Banker and Goslin, 1998). Thirdly, it must be able to be ink-jet printed reliably by meeting the previously mentioned constraints.

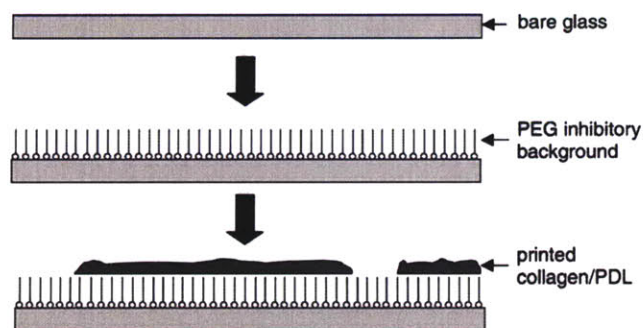


Fig. 4. Diagram of the surface patterning process. The bare glass was uniformly coated with a PEG inhibitory background. The amino-terminated PEG was covalently bonded to the glass surface via a three-step chemical process that used a glass-bonding aminosilane and the crosslinker glutaraldehyde. The adhesive collagen/PDL mixture was printed by ink-jet on top of the PEG background, leaving a pattern of cell-adhesive material that persisted for weeks in culture.

For the adhesive molecule, we chose to use a 25:1 mixture of collagen (4 mg/ml, Biosciences, BD 354236) and PDL (1 mg/ml, Sigma P0899). This mixture was diluted in water so that it was approximately 0.05% by weight. We found that this mixture was able to meet all three requirements described in the previous paragraph. In patterned culture, this mixture was ink-jet printed onto PEG-coated slides.

2.4. Cell culture

Cells from P1 rat hippocampi were obtained using a protocol similar to that which has been described elsewhere (Banker and Goslin, 1998). The dissection solution was HBSS (Sigma H2387) supplemented with 4 mM NaHCO₃ and 5 mM HEPES. Hippocampal tissue was proteolyzed for 40 min at 37°C, followed by trituration and washing. The digestion solution consisted of dissection solution plus 20 U/ml Papain (Worthington 3126), 0.5 mM EDTA, 1.5 mM CaCl₂, 1 mM L-cysteine, and 1 µg/ml DNase. 0.5 ml of the dissociated cell suspension was plated at 40,000–50,000 cells/ml onto a 12 mm coverslip inside a 24-well plate. The plating medium consisted of BME (Invitrogen 21010-046), 10 mM HEPES (pH 7.35), 1 mM Na-pyruvate, 6 mg/ml glucose, 10% FBS (Hyclone SH30071.02), Mito serum extender (Biosciences, BD 355006), and 2% B27 (Invitrogen 17504-044).

For the patterned cell population: Prior to plating, patterned coverslips were incubated in the culture medium overnight, which was aspirated before plating. We found this pre-plating incubation significantly increased our yield of healthy cells, perhaps because some residual toxicity from the PEG chemistry was reduced through this rinse. Another possible explanation is that the serum facilitated greater protein adsorption onto the printed collagen/PDL (Schaffner et al., 1995), but we did not investigate such mechanisms further. Four hours after plating, the plating medium was gently aspirated and replaced by a serum-free Neurobasal medium (Gibco/Invitrogen 12348-017) with 2% B27 and 0.25% glutamine (Brewer et al., 1993). The same serum-free medium was used for feeding (50% replacement every 4 days in vitro).

This replacement of standard culture medium with serum-free Neurobasal was intended to preserve pattern adherence; serum-containing culture medium is incompatible with this goal since glial growth is excessive when serum is present (Banker and Goslin, 1998; Wyart et al., 2002). We found that this culture protocol limited glial growth, as has been previously reported with the use of Neurobasal, while still preserving some glia in the culture (Brewer et al., 1993). Glia, which previously were thought of as passive support cells for neurons, have been found to actively control synaptogenesis, synapse number, and synaptic plasticity (see Haydon (2001) for a recent review). Thus, using Neurobasal, the population of glia was kept relatively low but extant. This improved pattern adherence and maintained the

neurons on-pattern in a more biologically-realistic manner than glia-free cultures.

We separately prepared low-density control cultures which did not include the cell-repulsive background or ink-jet printed cell adhesion molecules of the patterned cultures. In the low-density control cultures, neither overnight incubation in the culture medium prior to plating nor post-plating replacement of the culture medium was done. Since control cultures did not have patterns requiring adherence, they were plated on coverslips covered with an established astrocyte layer to increase neuron survivability. Control cultures were fed with culture medium containing serum (50% replacement every 4 days in vitro). All cells were maintained in an incubator with a 5% CO₂ atmosphere at 37°C.

2.5. Electrophysiology

We used the patch-clamp technique to measure several electrophysiological properties of the different cultured cells. For all cells, we continuously calculated and recorded access resistance, membrane resistance, and membrane capacitance. Patch recordings were made using a HEKA EPC 8 amplifier with a 5 kHz (eight pole Bessel) low-pass filter and custom software. All recordings were made between 10 and 12 days in vitro. During the recordings, the culture medium was replaced by an extracellular bath solution containing NaCl (145 mM), HEPES (10 mM), glucose (8 mM), KCl (3 mM), CaCl₂ (3 mM), and MgCl₂ (2 mM) with pH adjusted to 7.3. Pipettes made of borosilicate glass were pulled on a Flaming/Brown puller (Sutter Instruments) such that pipette resistance in the bath solution was kept between 3 and 7 MΩ. Pipettes contained K-gluconate (130 mM), KCL (10 mM), MgCl₂ (5 mM), EGTA (0.6 mM), HEPES (5 mM), CaCl₂ (0.06 mM), Mg-ATP (2 mM), GTP (0.2 mM), leupeptine (0.2 mM), phosphocreatine (20 mM), creatine phosphokinase (50 U/ml) (Arancio et al., 1995). Seals were always above 1 GΩ resistance and most often were several GΩ. Average access resistance was kept below 20 MΩ for all recordings.

2.6. Immunocytochemistry

Antibody staining was done using mouse monoclonal anti-GABA (1:200, Sigma A0310) and rabbit polyclonal anti-synapsin I (1:750, Chemicon AB1543) antibodies. Secondary antibodies from Molecular Probes were goat IgG anti-rabbit (Alexa Fluor 350, A-11046) and anti-mouse (Alexa Fluor 488, A-11001); both used at 1:200 dilution. Cells were first fixed for 20 min in a 4% formaldehyde solution, rinsed three times in PBS, and then permeabilized in a 0.25% Triton X solution. After a single rinse and then blocking in a 10% goat serum solution, cells were incubated overnight at 4°C with the primary antibody at the indicated concentration. Cells were then rinsed three times and incubated with secondary antibodies for 1 h. Again, cells were rinsed three times and stored at 4°C until analysis. As a

control, cells were incubated without the primary antibodies. Images were acquired using a CoolSnap HQ (Roper Scientific) CCD camera. Analysis was done using custom software. For GABAergic cell detection, we set an appropriate brightness threshold that was used for all images from a single plate and a minimum cell size to automate the process. Only when cells overlapped did we adjust cell counts accordingly. For synapsin I puncta detection, we applied a radial tophat filter to reduce distortion from light scattering and then manually counted puncta.

3. Results

All results reported are mean \pm standard deviation, unless indicated otherwise.

3.1. Island size scales with the number of droplets deposited

To design a pattern to print out as expected, it was necessary to know how many droplets were needed to print a certain island size. At a given X – Y location for the print head, an island was made by depositing multiple droplets in quick

succession (500 Hz) so that all droplets were deposited before any significant drying had occurred. The resulting hemisphere of liquid on the substrate, much larger than a single droplet, slowly dried until a circle of material remained. The size of a micro-island depended on the number of droplets deposited. Also, due to variation in the hydrophobicity of different substrates, the contact angle of the water with the substrate—and hence the resulting dot diameter—depended on the substrate being printed onto. Previous studies of dot morphology by atomic force microscopy (AFM) have indicated that more material is deposited around the edges of the droplet than in the middle (Fuller et al., 2002).

Micro-islands consisting of varying numbers of droplets of the collagen/PDL mixture were printed onto bare glass and onto PEG-coated glass to determine their sizes. Dried islands had enough solid material that they were visible in phase contrast microscopy and were measured using an eyepiece micrometer. Islands ranged in size from $65 \pm 5 \mu\text{m}$ in diameter for a single droplet of collagen/PDL mixture on PEG to $460 \pm 5 \mu\text{m}$ for 512 droplets (Fig. 5, $n = 8$). Results indicated that the dot diameter varied as the cube root of the number of droplets deposited, as expected. As shown, micro-islands are larger on glass, most likely due to the substrate's relatively higher hydrophilicity, and thus,

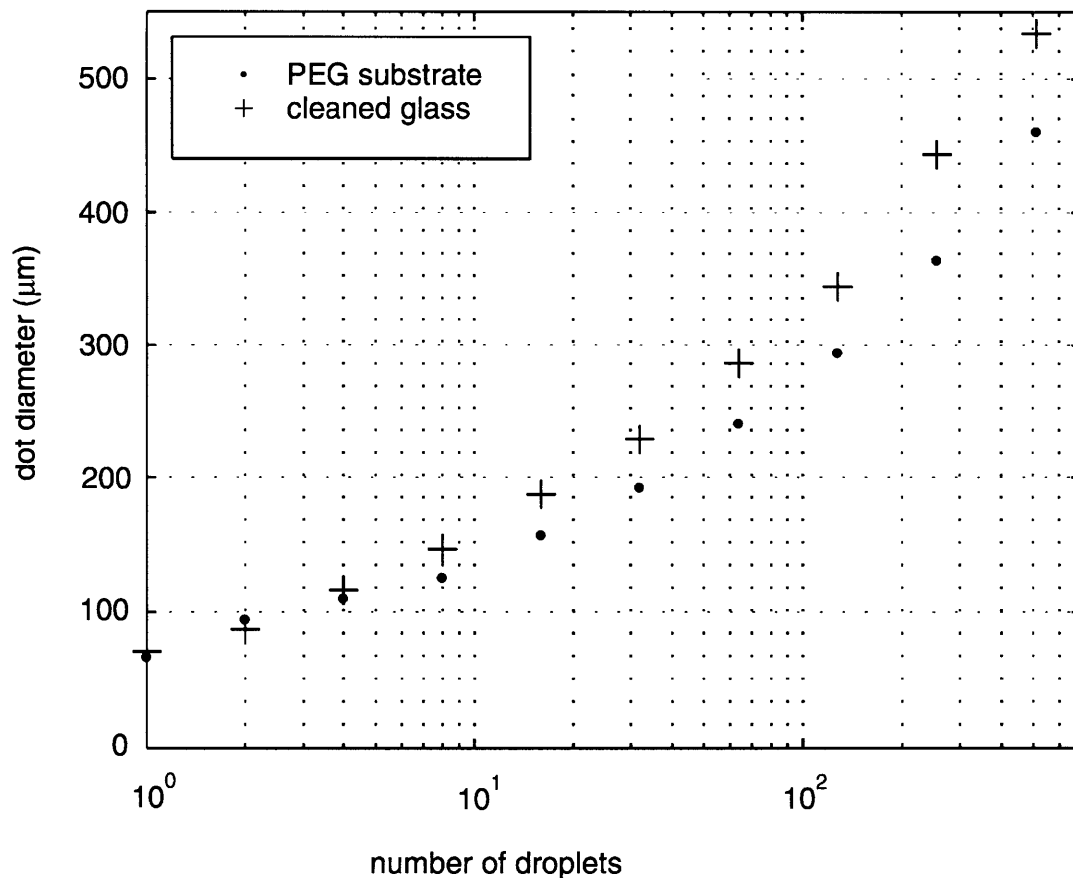


Fig. 5. Micro-island size scales with droplets deposited. For each data point, the ink-jet print head was placed at a single X – Y location and multiple droplets were deposited in quick succession (500 Hz) so that they were all deposited before any significant drying had occurred. The diameter of a micro-island grew slowly as the number of droplets deposited increased and also depended on the composition of the substrate being printed onto ($n = 8$).

lower droplet contact angles. We found that heating the substrate had little effect on the size of micro-islands (data not shown).

3.2. Arbitrary patterns can be printed

Lines of droplets were fabricated by depositing droplets sequentially at a sufficiently low speed such that each droplet had fully evaporated before the subsequent droplet was deposited. To expedite this process, the substrate was heated to 34°C and droplets were ejected at the rate of 1 Hz. Line-type printing structures were useful for making shapes other than micro-islands. When connecting a larger micro-island to

a line of droplets, it was important to deposit the island first, and then subsequently the line, to ensure that the relatively large volume of liquid in the micro-island was not wicked away into an oblong shape by a previously existing line of printed material. Patterns such as micro-islands, connected micro-islands, box shapes, and alphanumeric text were printed with the collagen/PDL mixture onto the repulsive PEG background (Fig. 6, left column).

An ink-jet printed pair of neighboring lines of droplets was printed with a gap of $8 \pm 2 \mu\text{m}$ between them and maintained for a distance of over a millimeter (data not shown). This small feature size suggests the ability of ink-jet printing to fabricate certain patterns much smaller

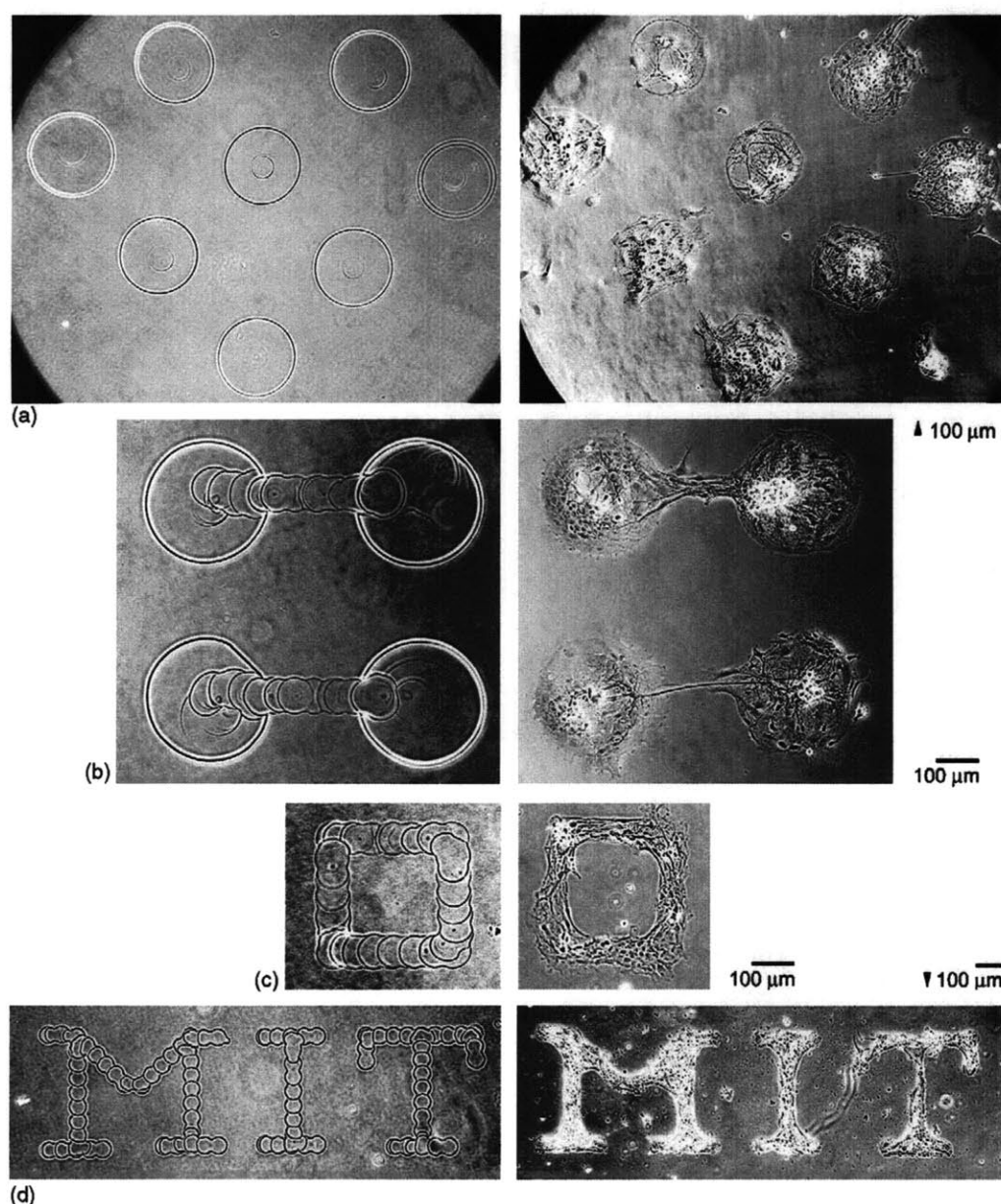


Fig. 6. Cells adhere to printed patterns. Left: collagen/PDL mixture printed onto a uniform PEG inhibitory background; right: cells adhered to patterns after 8–10 days in culture. Patterns include (a) an array of micro-islands 350 μm in diameter, (b) micro-islands connected by narrow channels 100 μm across, (c) a square, and (d) text.

than the diameter of a single droplet (65 μm for our print head and printing parameters) by printing in reverse. If the printed material were cell-repulsive, such as PEG, and if the unprinted areas were adhesive, then such small channels could be sufficiently small to only allow processes, not cell bodies, to grow inside the channels. This type of pattern was aided by the use of our custom hardware, which had a position repeatability of $\pm 1 \mu\text{m}$.

3.3. Cells retain pattern adhesion through 25 days in vitro

Neurons and glia plated onto the collagen/PDL on PEG patterns showed strong compliance to the printed patterns (Fig. 6, right column) after 8–10 days in culture and longer. In Fig. 7, we show some smaller islands with only one or two neurons on each island.

Confinement of plated neurons to micro-islands was quantified by phase-contrast imaging of cultures with 350 μm

diameter printed micro-islands (250 droplets) at days 5, 8, 10, 15, 20, and 25 in vitro. An intact micro-island had no neurons or processes making contact with other islands. The percentage of intact micro-islands was 75% after 5 days in vitro and stabilized to approximately 50% after 20 days. (Fig. 8).

3.4. Patterned cultures have normal passive membrane properties and resting potentials

A prerequisite for further studies with patterned culture is for the patterned neurons to display normal, healthy electrophysiological properties. To investigate this, we compared passive membrane properties and resting potentials of the cells grown on patterned substrates to those of the low-density, un-patterned cultures. We measured these properties in whole-cell mode of the patch-clamp amplifier and the results are given in Table 1.

Resting potentials were measured immediately after rupture. As shown in the table, patterned and control cultures had very similar mean resting potentials. Membrane capacitance and membrane resistance were measured using a 20 ms test pulse of 3 mV magnitude, repeated twice each second for a 5 min period to establish a stable value. Membrane resistance was somewhat higher in control cultures ($402 \pm 163 \text{ M}\Omega$) than in patterned cultures ($277 \pm 125 \text{ M}\Omega$) but the difference was not significant (independent *t*-test; $t(22) = 2.12$; $P > 0.01$). In both types of culture, membrane resistance varied greatly from cell to cell but always remained in the 100 $\text{M}\Omega$ to 1 $\text{G}\Omega$ range, as mentioned in previous reports (Evans et al., 1998; Wyart et al., 2002). We found that membrane capacitance was slightly higher in patterned cultures ($80 \pm 29 \text{ pF}$) than in control cultures ($57 \pm 20 \text{ pF}$) but also not significantly different ($t(22) = -2.15$; $P > 0.01$). Despite the small differences in mean membrane resistance and capacitance, membrane time constants, which are the product of membrane resistance and capacitance, were very similar in both patterned cultures ($19 \pm 6 \text{ ms}$) and control cultures ($21 \pm 5 \text{ ms}$) and the difference between the conditions was even less significant ($t(22) = 0.63$; $P > 0.05$).

3.5. Patterned cultures have similar distributions of GABAergic cells and synapsin I puncta as control cultures

We also wanted to compare the relative percentage of inhibitory and excitatory cells in our patterned cultures with classical, un-patterned culture. Since a majority of inhibitory cells in the hippocampus are GABAergic cells (Segal, 1991), immunoreactivity for GABA, which stains entire cell bodies and axons, is a good indicator of inhibitory cells. As seen in Fig. 9A, patterned cultures contain both GABAergic cells and non-GABAergic (most likely glutamatergic) cells. For our purposes, total cell counts were established in brightfield using differential interference contrast (DIC) microscopy and then GABAergic cells were counted by immunoreactivity for GABA, similar to previous studies (Benson et al., 1994). We found that 25% of neurons were GABAergic cells

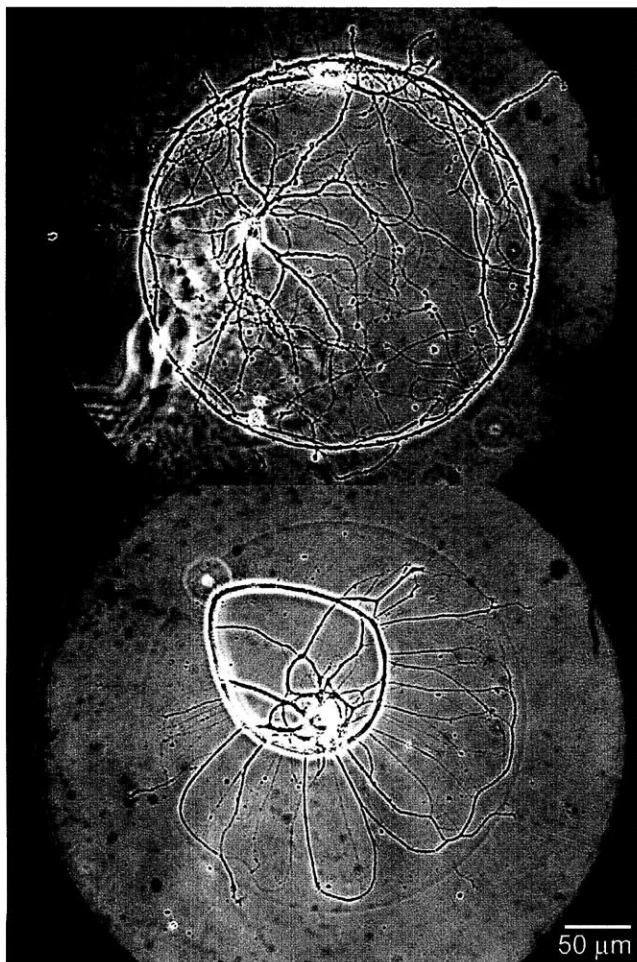


Fig. 7. Close-up of small numbers of neurons on printed micro-islands after 20 days in vitro. Top: a pair of neurons with processes encircling the border of the micro-island; bottom: a single neuron on an island. Its processes appear to have turned inward upon reaching the boundary between the collagen/PDL island and the PEG background.

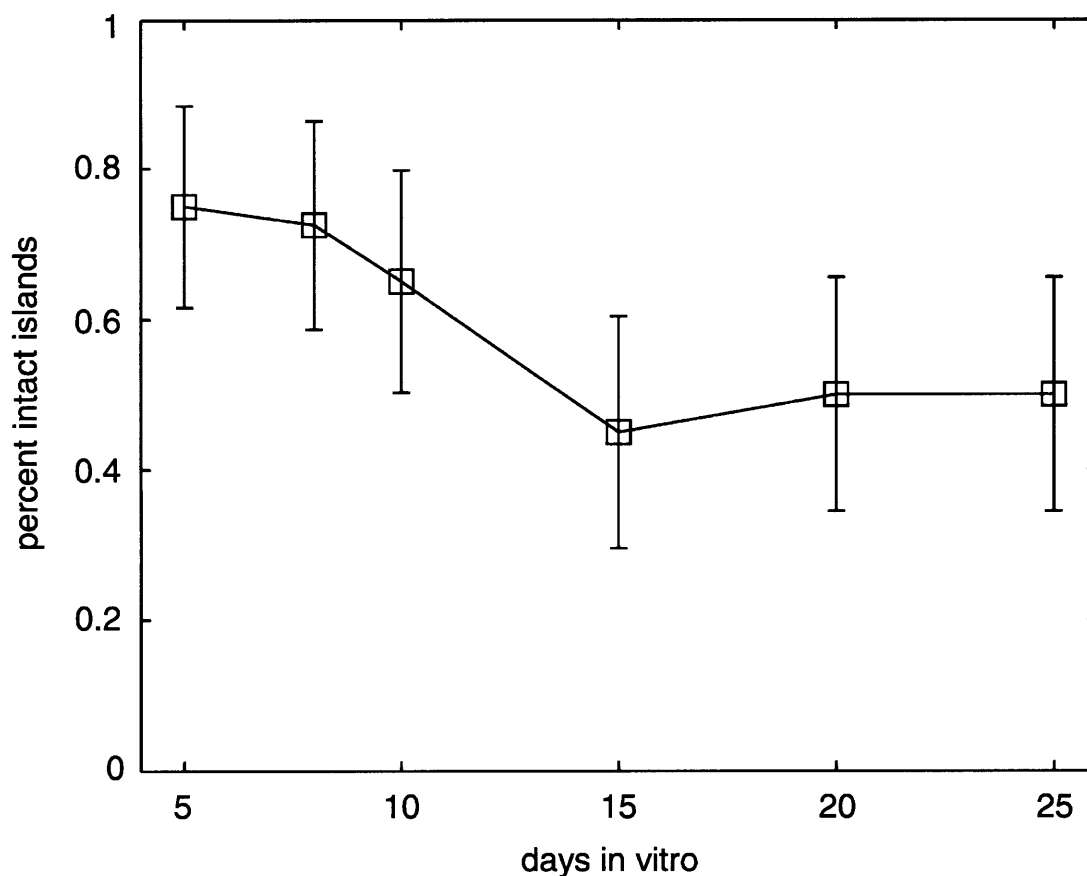


Fig. 8. Percentage of intact micro-islands. Islands were intact if no cells on the island made contact to other islands and not intact otherwise; 75% of islands were intact after 5 days in vitro and 50% were intact after 20 days ($n = 40$). Error bars denote 95% confidence intervals.

Table 1

Passive membrane properties of patterned cells and un-patterned control cells

	Resting potential (mV)	Membrane resistance ($M\Omega$)	Membrane capacitance (pF)	Membrane time constant (ms)
Control ($n = 12$)	−55.3 (8.1)	402 (163)	58 (20)	21 (5)
Pattern ($n = 12$)	−54.7 (6.6)	277 (125)	80 (29)	19 (6)

Resting potentials were measured immediately after rupture. The membrane time constant is a product of membrane resistance and capacitance. Patterned and control cultures had very similar mean resting potentials and membrane time constants. *Format*: mean (standard deviation).

in patterned cultures ($n = 308$ cells), in comparison to 33% GABAergic cells in control cultures ($n = 378$) (Fig. 9B). These percentages are not significantly different (chi-squares test, d.f. = 2; $P > 0.01$) and are comparable to previous results with hippocampal cell culture (Legido et al., 1990; Walker and Peacock, 1981).

We also compared the mean density of synapsin I puncta along axons in patterned and control cultures. Synapsins are abundant phosphoproteins found in virtually all presynaptic terminals (Greengard et al., 1993). Fig. 9C shows a sample synapsin I immunostaining of a single printed micro-island. In both pattern and control cultures, synapsin I immunoreactivity is distributed in distinct clusters, corresponding most likely to synapses in the cultures. Patterned cultures ($n = 253$ puncta) had an average of $2.95 \text{ puncta}/20 \mu\text{m}^2$ and control cultures ($n = 276$) had

an average of $2.29 \text{ puncta}/20 \mu\text{m}^2$ (Fig. 9D). These values are not significantly different (independent t -test; $t(46) = -2.46$; $P > 0.01$) and similar synaptic density results have been found in high-density, un-patterned hippocampal cultures (Renger et al., 2001).

4. Discussion

We have presented the design and operation of a novel ink-jet printer, pattern chemistry, and culture protocol that yields patterned neurons and glia. This is one of the first known applications of ink-jet printing to fabricating chemical patterns for neurons in culture (Roth et al., in press; Turcu et al., 2003). The method has advantages over other patterning techniques in that it is both programmable and relatively

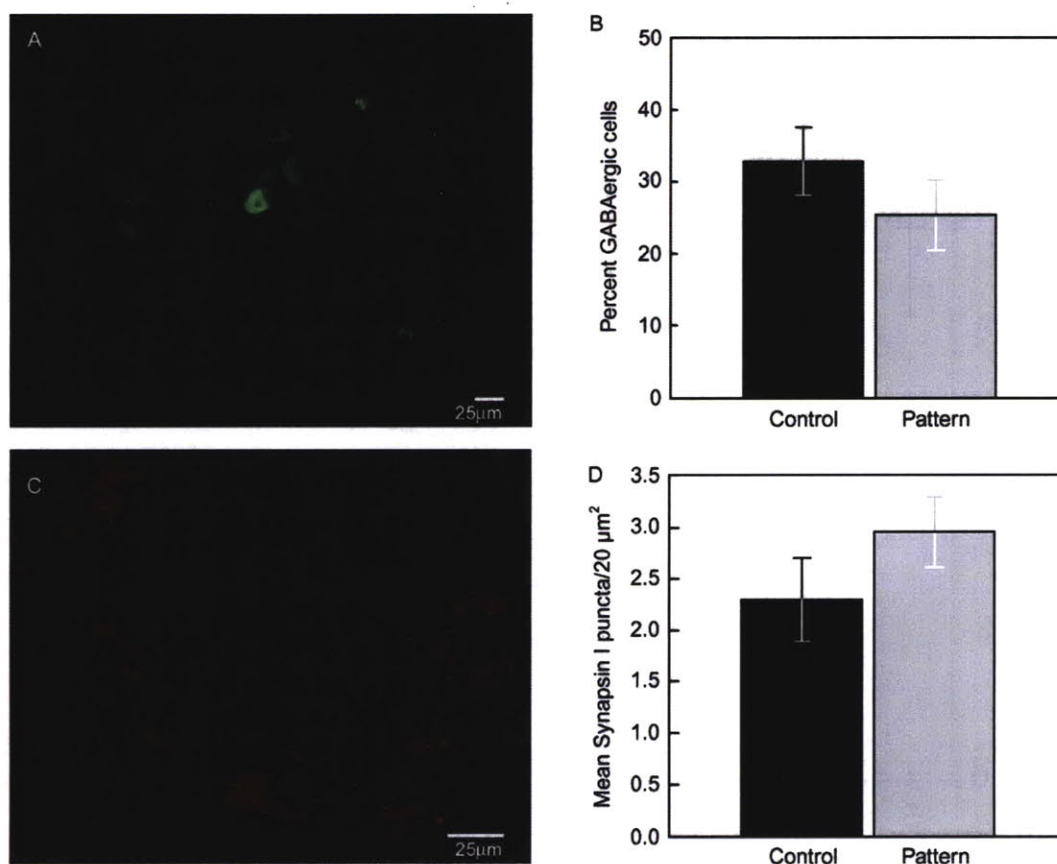


Fig. 9. Immunostaining for GABA and synapsin I. (A) A sample micro-island stained for GABA. (B) Comparison of the mean percentage of GABAergic cells in patterned ($n = 308$ cells) and un-patterned ($n = 378$) cultures. Percentages were estimated by counting cells with GABA immunoreactivity and counting all cells visible under brightfield DIC microscopy. (C) A sample micro-island stained for synapsin I. (D) Comparison of the mean density of synapsin I puncta per $20 \mu\text{m}^2$ in patterned ($n = 253$ puncta from 24 processes) and un-patterned ($n = 276$ puncta from 24 processes) cultures. In both graphs, error bars denoting 95% confidence intervals indicate that the difference between pattern and control culture populations is not significant.

inexpensive. In addition, ink-jet printing has other potential advantages for neuroscience including the ability to fabricate gradients, layered patterns, and non-planar structures much more easily than master pattern-based approaches. We expect dot size for the best, commercially-available ink-jet printing technology, which has been steadily decreasing but is fundamentally limited by fluid mechanics, to be roughly $30 \mu\text{m}$, which is lower than the $65 \mu\text{m}$ resolution demonstrated here. Newer technologies in drop generation based on print heads different than the kind used in this work, such as acoustic droplet generators, may push this result even lower in the future but printing reliability (e.g. frequency of clogging) will have to be addressed.

The surface chemistry presented uses a uniform, covalently-bonded layer of PEG as the inhibitory background and a collagen/PDL mixture printed on top as the cell-adhesive foreground. In principle, this chemistry also has the flexibility to be reversed, such that the PEG is printed atop a reactive surface of aldehyde groups and then is washed briefly with the adhesive collagen/PDL. Patterns for neurons included controlled micro-islands, lines of dots as narrow as $65 \mu\text{m}$, gaps as small as $8 \pm 2 \mu\text{m}$, and arbitrary shapes. Cell adhesion to micro-islands was com-

parable to previous techniques (Branch et al., 2000) and our electrophysiological and immunocytochemical investigations indicated that patterned cultures also displayed similar properties to classical, un-patterned low-density cultures. These results demonstrate that ink-jet printing can be used to fabricate chemical patterns that are neuron-compatible, and we suggest that the technology may prove to be useful for a range of studies on neurons in vitro.

Our recommendations are the following. For making simple, relatively low-resolution patterns, we can recommend the use of an inexpensive desktop printer and a cartridge refill kit filled with the desired biomolecule to print onto coverslips taped to sheets of regular paper (Klebe, 1988; Roda et al., 2000). We expect resolution to be lower than that demonstrated here because of less control over driver software and over the positioning precision of the head. However, such an approach would leverage sophisticated drawing software for the PC and would be sufficient to do the PDL/collagen printing on PEG reported here. A more high-end solution could use relatively expensive research-grade hardware that has been recently released for such applications (e.g. Jetlab™ II, MicroFab Technologies), or a custom-built solution such as is reported here.

Lastly, there are certain tasks which might be better suited to patterning techniques that are based on a single master pattern, but we believe these are limited because the need to change patterns is likely to arise often during experimental work. The relatively slow printing speed employed in this work for the smallest lines (one drop per second, to ensure complete drying between adjoining droplets) resulted in printing times of about 5 min per coverslip for most of the patterns used in this work, making the hardware less suitable for complex or repeating patterns. Such patterning might be better suited to photolithography or stamping.

Lastly, we believe there are many other applications for ink-jet patterning with neural cell culture. The effects of many extracellular matrix proteins and other non-endogenous signaling molecules could be tested in a combinatoric fashion using ink-jet patterning. It may be possible to print actual neurons through the print head, but problems with drying out of the neurons or changing osmolarity with evaporation during printing would have to be addressed. We have already used our printer to create three-dimensional structures, such as walls and tunnels from hot-melt wax, and substrate-bound gradients of laminin (unpublished data). We believe these preliminary results represent the future of the body of work reported here. Printed patterns and gradients of neurotrophic factors could facilitate in vitro studies of axon guidance, target selection and cell maturation during neural development. The potential ease of printing substrate-bound gradients—by printing varying numbers of layers of very low-concentration ink—connected to other arbitrary patterns could be a major advantage of ink-jet patterning, since many neurotrophic factors and their receptors have already been shown to use such gradients (Bonhoeffer and Huf, 1982; Dertinger et al., 2002; Houchmandzadeh et al., 2002; Sperry, 1963).

Acknowledgements

We are grateful to Professor H. Sebastian Seung (MIT Department of Brain and Cognitive Science), Dr. Shuguang Zhang (MIT Center for Biomedical Engineering), and Professor Joseph Jacobson (MIT Media Laboratory) for guidance, resources, and Lab space. We are indebted to Jung Choi for his dedication and outstanding results with neuron culture. We are grateful to Emily Hueske for multiple, insightful discussions about immunocytochemistry, to Shuwang An for assistance with surface chemistry procedures, to Thomas Griffiths for statistical advice, and to Guosong Liu, Bing Li, and Yuki Goda for guidance with culture techniques. Adrien Desjardins, David Kleinfeld, Venkatesh Murthy, Bayle Shanks, Nathan Wilson and an anonymous reviewer provided valuable comments on various drafts of the manuscript. NES is supported by a HHMI Predoctoral Fellowship. SBF is supported by a NSF Graduate Fellowship. This work was funded by the Defense Advanced Project Research Agency/BioComp, NSF

CCR-0122419 to MIT's Media Laboratory Center for Bits and Atoms for the printer, and a Whitaker Foundation grant to Shuguang Zhang. H. Sebastian Seung is funded by the David and Lucille Packard Foundation and the Howard Hughes Medical Institute.

References

- Arancio O, Kandel ER, Hawkins RD. Activity-dependent long-term enhancement of transmitter release by presynaptic 3', 5'-cyclic GMP in cultured hippocampal neurons. *Nature* 1995;376:74–80.
- Banker G, Goslin K. *Culturing nerve cells*. 2nd ed. Cambridge, Mass: MIT Press, 1998.
- Benson DL, Watkins FH, Steward O, Banker G. Characterization of GABAergic neurons in hippocampal cell cultures. *J Neurocytol* 1994;23:279–95.
- Bonhoeffer F, Huf J. In vitro experiments on axon guidance demonstrating an anterior-posterior gradient on the tectum. *Embo J* 1982;1:427–31.
- Branch DW, Wheeler BC, Brewer GJ, Leckband DE. Long-term maintenance of patterns of hippocampal pyramidal cells on substrates of polyethylene glycol and microstamped polylysine. *IEEE Trans Biomed Eng* 2000;47:290–300.
- Brewer GJ, Torricelli JR, Evege EK, Price PJ. Optimized survival of hippocampal neurons in B27-supplemented Neurobasal, a new serum-free medium combination. *J Neurosci Res* 1993;35:567–76.
- Cass T, Ligler FS. *Immobilized biomolecules in analysis: a practical approach*. Oxford: Oxford University Press, 1998.
- Dertinger SK, Jiang X, Li Z, Murthy VN, Whitesides GM. Gradients of substrate-bound laminin orient axonal specification of neurons. *Proc Natl Acad Sci USA* 2002;99:12542–7.
- Evans MS, Collings MA, Brewer GJ. Electrophysiology of embryonic, adult and aged rat hippocampal neurons in serum-free culture. *J Neurosci Methods* 1998;79:37–46.
- Fuller SB, Jacobson JM. Ink-jet fabricated nanoparticle micro-electromechanical systems. In: *Proceedings of the IEEE conference on micro-electromechanical systems*, 2000; pp. 138–41.
- Fuller SB, Wilhelm EJ, Jacobson JA. Ink-jet printed nanoparticle microelectromechanical systems. *J Microelectromech Sys* 2002;11:54–60.
- Furshpan EJ, MacLeish PR, O'Lague PH, Potter DD. Chemical transmission between rat sympathetic neurons and cardiac myocytes developing in microcultures: evidence for cholinergic, adrenergic, and dual-function neurons. *Proc Natl Acad Sci USA* 1976;73:4225–9.
- Greengard P, Valtorta F, Czernik AJ, Benfenati F. Synaptic vesicle phosphoproteins and regulation of synaptic function. *Science* 1993;259:780–5.
- Griffith LG, Wu B, Cima MJ, Powers MJ, Chagnaud B, Vacanti JP. In vitro organogenesis of liver tissue. *Ann NY Acad Sci* 1997;831:382–97.
- Haydon PG. GLIA: listening and talking to the synapse. *Nat Rev Neurosci* 2001;2:185–93.
- Heinzl J, Herz CH. Ink-jet printing. *Adv Electron Electron Phys* 1985;65:91–171.
- Hickman JJ, Bhatia SK, Quong JN, Shoen P, Stenger DA, Pike CJ, Cotman CW. Rational pattern design for in-vitro cellular networks using surface photochemistry. *J Vac Sci Technol Vac Surf Films* 1994;12:607–16.
- Holmes TC, de Lacalle S, Su X, Liu G, Rich A, Zhang S. Extensive neurite outgrowth and active synapse formation on self-assembling peptide scaffolds. *Proc Natl Acad Sci USA* 2000;97:6728–33.
- Houchmandzadeh B, Wieschaus E, Leibler S. Establishment of developmental precision and proportions in the early *Drosophila* embryo. *Nature* 2002;415:798–802.
- Klebe RJ. Cytoscribing: a method for micropositioning cells and the construction of two- and three-dimensional synthetic tissues. *Exp Cell Res* 1988;179:362–73.

- Kleinfeld D, Kahler KH, Hockberger PE. Controlled outgrowth of dissociated neurons on patterned substrates. *J Neurosci* 1988;8:4098–120.
- Legido A, Reichlin S, Dichter MA, Buchhalter J. Expression of somatostatin and GABA immunoreactivity in cultures of rat hippocampus. *Peptides* 1990;11:103–9.
- Martinoia S, Bove M, Tedesco M, Margesin B, Grattarola M. A simple microfluidic system for patterning populations of neurons on silicon micromachined substrates. *J Neurosci Methods* 1999;87:35–44.
- Renger JJ, Egles C, Liu G. A developmental switch in neurotransmitter flux enhances synaptic efficacy by affecting AMPA receptor activation. *Neuron* 2001;29:469–84.
- Roda A, Guardigli M, Russo C, Pasini P, Baraldini M. Protein microdeposition using a conventional ink-jet printer. *Biotechniques* 2000;28:492–6.
- Roth EA, Xu T, Das M, Gregory C, Hickman JJ, Boland T. Inkjet printing for high-throughput cell patterning. *Biomaterials*, in press.
- Sachlos E, Reis N, Ainsley C, Derby B, Czernuszka JT. Novel collagen scaffolds with predefined internal morphology made by solid freeform fabrication. *Biomaterials* 2003;24:1487–97.
- Schaffner AE, Barker JL, Stenger DA, Hickman JJ. Investigation of the factors necessary for growth of hippocampal neurons in a defined system. *J Neurosci Methods* 1995;62:111–9.
- Scholl M, Sprossler C, Denyer M, Krause M, Nakajima K, Maelicke A, Knoll W, Offenhausser A. Ordered networks of rat hippocampal neurons attached to silicon oxide surfaces. *J Neurosci Methods* 2000;104:65–75.
- Segal MM. Epileptiform activity in microcultures containing one excitatory hippocampal neuron. *J Neurophysiol* 1991;65:761–70.
- Sperry RW. Chemoaffinity in the orderly growth of nerve fiber patterns and connections. *Proc Natl Acad Sci USA* 1963;50:703–10.
- St John PM, Kam L, Turner SW, Craighead HG, Issacson M, Turner JN, Shain W. Preferential glial cell attachment to microcontact printed surfaces. *J Neurosci Methods* 1997;75:171–7.
- Turcu F, Tratsk-Nitz K, Thanos S, Schuhmann W, Heiduschka P. Ink-jet printing for micropattern generation of laminin for neuronal adhesion. *J Neurosci Methods* 2003;131:141–8.
- Walker CR, Peacock JH. Development of GABAergic function of dissociated hippocampal cultures from fetal mice. *Brain Res* 1981;254:541–55.
- Watanabe K, Miyazaki T, Matsuda R. Growth factor array fabrication using a color ink jet printer. *Zoolog Sci* 2003;20:429–34.
- Westermarck B. Growth control in miniclones of human glial cells. *Exp Cell Res* 1978;111:295–9.
- Wheeler BC, Corey JM, Brewer GJ, Branch DW. Microcontact printing for precise control of nerve cell growth in culture. *J Biomech Eng* 1999;121:73–8.
- Wilson Jr WC, Boland T. Cell and organ printing 1: protein and cell printers. *Anat Rec* 2003;272A:491–6.
- Wyart C, Ybert C, Bourdieu L, Herr C, Prinz C, Chatenay D. Constrained synaptic connectivity in functional mammalian neuronal networks grown on patterned surfaces. *J Neurosci Methods* 2002;117:123–31.
- Zhang S, Holmes T, Lockshin C, Rich A. Spontaneous assembly of a self-complementary oligopeptide to form a stable macroscopic membrane. *Proc Natl Acad Sci USA* 1993;90:3334–8.
- Zhang S, Holmes TC, DiPersio CM, Hynes RO, Su X, Rich A. Self-complementary oligopeptide matrices support mammalian cell attachment. *Biomaterials* 1995;16:1385–93.
- Zhang SG, Yan L, Altman M, Lassle M, Nugent H, Frankel F, Lauffenburger DA, Whitesides GM, Rich A. Biological surface engineering: a simple system for cell pattern formation. *Biomaterials* 1999;20:1213–20.

Bibliography

- Abeles M, Bergman H, Gat I, Meilijson I, Seidemann E, Tishby N, Vaadia E (1995) Cortical activity flips among quasi-stationary states. *Proc Natl Acad Sci U S A* 92:8616–20.
- Ahmari SE, Buchanan J, Smith SJ (2000) Assembly of presynaptic active zones from cytoplasmic transport packets. *Nat Neurosci* 3:445–51.
- Aletta JM, Greene LA (1988) Growth cone configuration and advance: a time-lapse study using video-enhanced differential interference contrast microscopy. *J Neurosci* 8:1425–35.
- Argiro V, Bunge MB, Johnson MI (1984) Correlation between growth form and movement and their dependence on neuronal age. *J Neurosci* 4:3051–62.
- Argiro V, Bunge MB, Johnson MI (1985) A quantitative study of growth cone filopodial extension. *J Neurosci Res* 13:149–62.
- Argiro V, Johnson M (1982) Patterns and kinetics of neurite extension from sympathetic neurons in culture are age dependent. *Journal of Neuroscience* 2:503–512.
- Bamburg JR, Bray D, Chapman K (1986) Assembly of microtubules at the tip of growing axons. *Nature* 321:788–90.
- Banker G, Goslin K (1998) *Culturing nerve cells* MIT Press, Cambridge, Mass., 2nd edition.
- Barnett EM, Cassell MD, Perlman S (1993) Two neurotropic viruses, herpes simplex virus type 1 and mouse hepatitis virus, spread along different neural pathways from the main olfactory bulb. *Neuroscience* 57:1007–25.
- Bearer EL, Reese TS (1999) Association of actin filaments with axonal microtubule tracts. *J Neurocytol* 28:85–98.
- Benhamou S (2004) How to reliably estimate the tortuosity of an animal’s path: straightness, sinuosity, or fractal dimension? *J Theor Biol* 229:209–20.
- Braitenberg V, Schüz A (1998) *Cortex: statistics and geometry of neuronal connectivity* Springer, Berlin, 2nd thoroughly rev. ed edition.
- Bray D (1970) Surface movements during the growth of single explanted neurons. *Proc Natl Acad Sci U S A* 65:905–10.

- Bray D (1973) Branching patterns of individual sympathetic neurons in culture. *The Journal of Cell Biology* 56:702–712.
- Bray D (1979) Mechanical tension produced by nerve cells in tissue culture. *J Cell Sci* 37:391–410.
- Bray D (1996) The dynamics of growing axons. membrane biophysics. *Curr Biol* 6:241–3.
- Bray D, Chapman K (1985) Analysis of microspike movements on the neuronal growth cone. *J Neurosci* 5:3204–13.
- Brewer GJ, Torricelli JR, Evege EK, Price PJ (1993) Optimized survival of hippocampal neurons in b27-supplemented neurobasal, a new serum-free medium combination. *J Neurosci Res* 35:567–76.
- Card JP, Enquist LW, Miller AD, Yates BJ (1997) Differential tropism of pseudorabies virus for sensory neurons in the cat. *J Neurovirol* 3:49–61.
- Caudy M, Bentley D (1986) Pioneer growth cone steering along a series of neuronal and non-neuronal cues of different affinities. *J Neurosci* 6:1781–95.
- Cheng HJ, Nakamoto M, Bergemann AD, Flanagan JG (1995) Complementary gradients in expression and binding of elf-1 and mek4 in development of the topographic retinotectal projection map. *Cell* 82:371–81.
- Craig AM (1998) Transfecting cultured neurons In Banker G, Goslin K, editors, *Culturing Nerve Cells*, pp. 79–111. MIT Press, Cambridge, MA, 2nd ed. edition.
- de Gennes PG (2007) Collective neuronal growth and self organization of axons. *Proc Natl Acad Sci U S A* 104:4904–6.
- Dent EW, Gertler FB (2003) Cytoskeletal dynamics and transport in growth cone motility and axon guidance. *Neuron* 40:209–27.
- Dent EW, Kalil K (2001) Axon branching requires interactions between dynamic microtubules and actin filaments. *J Neurosci* 21:9757–69.
- Dent EW, Tang F, Kalil K (2003) Axon guidance by growth cones and branches: common cytoskeletal and signaling mechanisms. *Neuroscientist* 9:343–53.
- Feng G, Mellor RH, Bernstein M, Keller-Peck C, Nguyen QT, Wallace M, Nerbonne JM, Lichtman JW, Sanes JR (2000) Imaging neuronal subsets in transgenic mice expressing multiple spectral variants of gfp. *Neuron* 28:41–51.
- George EB, Schneider BF, Lasek RJ, Katz MJ (1988) Axonal shortening and the mechanisms of axonal motility. *Cell Motil Cytoskeleton* 9:48–59.
- Goldberg DJ, Burmeister DW (1986) Stages in axon formation: observations of growth of aplasia axons in culture using video-enhanced contrast-differential interference contrast microscopy. *J Cell Biol* 103:1921–31.

- Goodhill GJ (1997) Diffusion in axon guidance. *Eur J Neurosci* 9:1414–21.
- Goodhill GJ (1998) Mathematical guidance for axons. *Trends Neurosci* 21:226–31.
- Goodhill GJ, Urbach JS (1999) Theoretical analysis of gradient detection by growth cones. *J Neurobiol* 41:230–41.
- Gottfried B (2007) Characterising straightness qualitatively In Fabrikant SI WM, editor, *The European Information Society: Leading the Way with Geo-information*, Lecture Notes in Geoinformation and Cartography. Springer, Berlin, Germany.
- Halloran MC, Kalil K (1994) Dynamic behaviors of growth cones extending in the corpus callosum of living cortical brain slices observed with video microscopy. *J Neurosci* 14:2161–77.
- Hamelryck T, Kent JT, Krogh A (2006) Sampling realistic protein conformations using local structural bias. *PLoS Computational Biology* 2:e131.
- Heacock AM, Agranoff BW (1977) Clockwise growth of neurites from retinal explants. *Science* 198:64–6.
- Hentschel HG, van Ooyen A (1999) Models of axon guidance and bundling during development. *Proc Biol Sci* 266:2231–8.
- Hiramoto Y, Baba S (1978) A quantitative analysis of flagellar movement in echinoderm spermatozoa. *Journal of Experimental Biology* 76:85–104.
- Hockberger PE (2002) A history of ultraviolet photobiology for humans, animals and microorganisms. *Photochem Photobiol* 76:561–79.
- Hockberger PE, Skimina TA, Centonze VE, Lavin C, Chu S, Dadras S, Reddy JK, White JG (1999) Activation of flavin-containing oxidases underlies light-induced production of h₂o₂ in mammalian cells. *Proc Natl Acad Sci U S A* 96:6255–60.
- Hughes A (1953) The growth of embryonic neurites; a study of cultures of chick neural tissues. *J Anat* 87:150–62.
- Imondi R, Kaprielian Z (2001) Commissural axon pathfinding on the contralateral side of the floor plate: a role for b-class ephrins in specifying the dorsoventral position of longitudinally projecting commissural axons. *Development* 128:4859–71.
- Jelinek F (1997) *Statistical methods for speech recognition* Language, speech, and communication. MIT Press, Cambridge, Mass.
- Juang BH, Rabiner LR (1990) The segmental k-means algorithm for estimating parameters of hidden markov-models. *Ieee Transactions on Acoustics Speech and Signal Processing* 38:1639–1641.
- Kaech S, Banker G (2006) Culturing hippocampal neurons. *Nat Protoc* 1:2406–15.

- Kalil K (1996) Growth cone behaviors during axon guidance in the developing cerebral cortex. *Prog Brain Res* 108:31–40.
- Kalil K, Szebenyi G, Dent EW (2000) Common mechanisms underlying growth cone guidance and axon branching. *J Neurobiol* 44:145–58.
- Katz MJ (1985a) Axonal branch shapes. *Brain Res* 361:70–6.
- Katz MJ (1985b) How straight do axons grow? *J Neurosci* 5:589–95.
- Katz MJ, George EB (1985) Fractals and the analysis of growth paths. *Bull Math Biol* 47:273–86.
- Katz MJ, George EB, Gilbert LJ (1984) Axonal elongation as a stochastic walk. *Cell Motil* 4:351–70.
- Krogh A, Larsson B, von Heijne G, Sonnhammer E (2001) Predicting transmembrane protein topology with a hidden markov model: application to complete genomes. *Journal of Molecular Biology* 305:567–580.
- Krottje JK, van Ooyen A (2007) A mathematical framework for modeling axon guidance. *Bull Math Biol* 69:3–31.
- Kuang RZ, Kalil K (1994) Development of specificity in corticospinal connections by axon collaterals branching selectively into appropriate spinal targets. *J Comp Neurol* 344:270–82.
- Langbein W, Leopold L (1966) River meanders–theory of minimum variance. *U.S. Geological Survey Professional Paper* 422-H.
- Langford GM (2001) Video-enhanced microscopy for analysis of cytoskeleton structure and function In Gavin RH, editor, *Cytoskeleton methods and protocols*, Methods in Molecular Biology, pp. 31–44. Humana Press, Totowa, N.J.
- Lohof AM, Quillan M, Dan Y, Poo MM (1992) Asymmetric modulation of cytosolic camp activity induces growth cone turning. *J Neurosci* 12:1253–61.
- Maskery S, Shinbrot T (2005) Deterministic and stochastic elements of axonal guidance. *Annu Rev Biomed Eng* 7:187–221.
- Maskery SM, Buettner HM, Shinbrot T (2004) Growth cone pathfinding: a competition between deterministic and stochastic events. *BMC Neurosci* 5:22.
- McAllister AK (2000) Biolistic transfection of neurons. *Sci STKE* 2000:PL1.
- Meyer MP, Smith SJ (2006) Evidence from in vivo imaging that synaptogenesis guides the growth and branching of axonal arbors by two distinct mechanisms. *J Neurosci* 26:3604–14.
- Ming GL, Song HJ, Berninger B, Holt CE, Tessier-Lavigne M, Poo MM (1997) camp-dependent growth cone guidance by netrin-1. *Neuron* 19:1225–35.

- Ming GL, Wong ST, Henley J, Yuan XB, Song HJ, Spitzer NC, Poo MM (2002) Adaptation in the chemotactic guidance of nerve growth cones. *Nature* 417:411–8.
- Montague PR, Friedlander MJ (1989) Expression of an intrinsic growth strategy by mammalian retinal neurons. *Proc Natl Acad Sci U S A* 86:7223–7.
- Myers PZ, Eisen JS, Westerfield M (1986) Development and axonal outgrowth of identified motoneurons in the zebrafish. *J Neurosci* 6:2278–89.
- Nakamura H, O’Leary D (1989) Inaccuracies in initial growth and arborization of chick retinotectal axons followed by course corrections and axon remodeling to develop topographic order. *Journal of Neuroscience* 9:3776–3795.
- O’Connor TP, Duerr JS, Bentley D (1990) Pioneer growth cone steering decisions mediated by single filopodial contacts in situ. *J Neurosci* 10:3935–46.
- Odde DJ, Tanaka EM, Hawkins SS, Buettner HM (1996) Stochastic dynamics of the nerve growth cone and its microtubules during neurite outgrowth. *Biotechnol Bioeng* 50:452–61.
- Okabe M, Ikawa M, Kominami K, Nakanishi T, Nishimune Y (1997) ‘green mice’ as a source of ubiquitous green cells. *FEBS Lett* 407:313–9.
- Okabe S, Hirokawa N (1990) Turnover of fluorescently labelled tubulin and actin in the axon. *Nature* 343:479–82.
- O’Leary DD, Bicknese AR, De Carlos JA, Heffner CD, Koester SE, Kutka LJ, Terashima T (1990) Target selection by cortical axons: alternative mechanisms to establish axonal connections in the developing brain. *Cold Spring Harb Symp Quant Biol* 55:453–68.
- O’Rourke NA, Fraser SE (1990) Dynamic changes in optic fiber terminal arbors lead to retinotopic map formation: an in vivo confocal microscopic study. *Neuron* 5:159–71.
- Portera-Cailliau C, Weimer RM, De Paola V, Caroni P, Svoboda K (2005) Diverse modes of axon elaboration in the developing neocortex. *PLoS Biol* 3:e272.
- Price JH, Gough DA (1994) Comparison of phase-contrast and fluorescence digital autofocus for scanning microscopy. *Cytometry* 16:283–97.
- Rabiner L (1989) A tutorial on hidden markov models and selected applications in speech recognition. *Proceedings of the IEEE* 77:257–286.
- Radons G, Becker JD, Dulfer B, Kruger J (1994) Analysis, classification, and coding of multielectrode spike trains with hidden markov models. *Biol Cybern* 71:359–73.
- Renger JJ, Egles C, Liu G (2001) A developmental switch in neurotransmitter flux enhances synaptic efficacy by affecting ampa receptor activation. *Neuron* 29:469–84.
- Risling M, Dalsgaard CJ, Cukierman A, Cuello AC (1984) Electron microscopic and immunohistochemical evidence that unmyelinated ventral root axons make u-turns or enter the spinal pia mater. *J Comp Neurol* 225:53–63.

- Rosoff WJ, Urbach JS, Esrick MA, McAllister RG, Richards LJ, Goodhill GJ (2004) A new chemotaxis assay shows the extreme sensitivity of axons to molecular gradients. *Nat Neurosci* 7:678–82.
- Ruthazer ES, Li J, Cline HT (2006) Stabilization of axon branch dynamics by synaptic maturation. *J Neurosci* 26:3594–603.
- Sabry JH, O'Connor TP, Evans L, Toroian-Raymond A, Kirschner M, Bentley D (1991) Microtubule behavior during guidance of pioneer neuron growth cones in situ. *J Cell Biol* 115:381–95.
- Sandmann D, Boycott BB, Peichl L (1996) Blue-cone horizontal cells in the retinae of horses and other equidae. *J Neurosci* 16:3381–96.
- Sanjana NE, Fuller SB (2004) A fast flexible ink-jet printing method for patterning dissociated neurons in culture. *J Neurosci Methods* 136:151–163.
- Schmitz C, Kinge P, Hutter H (2007) Axon guidance genes identified in a large-scale RNAi screen using the RNAi-hypersensitive *Caenorhabditis elegans* strain *nre-1(hd20) lin-15b(hd126)*. *Proceedings of the National Academy of Sciences* 104:834–839.
- Sepp KJ, Hong P, Lizarraga SB, Liu JS, Mejia LA, Walsh CA, Perrimon N (2008) Identification of neural outgrowth genes using genome-wide RNAi. *PLoS Genet* 4:e1000111.
- Shefi O, Harel A, B. Chklovskii D, Ben-Jacob E, Ayali A (2004) Biophysical constraints on neuronal branching. *Neurocomputing* 58:487–495.
- Shim S, Yuan JP, Kim JY, Zeng W, Huang G, Milshteyn A, Kern D, Muallem S, Ming GL, Worley PF (2009) Peptidyl-prolyl isomerase *fkbp52* controls chemotropic guidance of neuronal growth cones via regulation of *trpc1* channel opening. *Neuron* 64:471–83.
- Sonnhammer E, von Heijne G, Krogh A (1998) A hidden markov model for predicting transmembrane helices in protein sequences In *Proc. Int. Conf. Intell. Syst. Mol. Biol*, Vol. 6, pp. 175–182.
- Sperry R (1963) Chemoaffinity in the orderly growth of nerve fiber patterns and connections. *Proceedings of the National Academy of Sciences* 50:703–710.
- Stepanyants A, Tamás G, Chklovskii DB (2004) Class-specific features of neuronal wiring. *Neuron* 43:251–9.
- Szebenyi G, Callaway J, Dent E, Kalil K (1998) Interstitial branches develop from active regions of the axon demarcated by the primary growth cone during pausing behaviors. *Journal of Neuroscience* 18:7930–7940.
- Tanaka E, Ho T, Kirschner MW (1995) The role of microtubule dynamics in growth cone motility and axonal growth. *J Cell Biol* 128:139–55.
- Tanaka E, Kirschner MW (1995) The role of microtubules in growth cone turning at substrate boundaries. *J Cell Biol* 128:127–37.

- Tanaka EM, Kirschner MW (1991) Microtubule behavior in the growth cones of living neurons during axon elongation. *J Cell Biol* 115:345–63.
- Tang F, Dent EW, Kalil K (2003) Spontaneous calcium transients in developing cortical neurons regulate axon outgrowth. *J Neurosci* 23:927–36.
- Thanos S, Bonhoeffer F (1987) Axonal arborization in the developing chick retinotectal system. *J Comp Neurol* 261:155–64.
- Thomson AM, Morris OT (2002) Selectivity in the inter-laminar connections made by neocortical neurones. *J Neurocytol* 31:239–46.
- Turchin P (1996) Fractal analyses of animal movement: A critique. *Ecology(Durham)* 77:2086–2090.
- Van Essen DC (1997) A tension-based theory of morphogenesis and compact wiring in the central nervous system. *Nature* 385:313–8.
- Walter J, Kern-Veits B, Huf J, Stolze B, Bonhoeffer F (1987) Recognition of position-specific properties of tectal cell membranes by retinal axons in vitro. *Development* 101:685–96.
- Wen Q, Chklovskii DB (2005) Segregation of the brain into gray and white matter: a design minimizing conduction delays. *PLoS Comput Biol* 1:e78.
- Williamson T, Gordon-Weeks PR, Schachner M, Taylor J (1996) Microtubule reorganization is obligatory for growth cone turning. *Proc Natl Acad Sci U S A* 93:15221–6.